https://www.mediresonline.org/

MEDIRES Symbol of Quality Research

ISSN: 2836-5062

Open Access

Journal of Clinical Oncology Reports

Research Article

Mitochondrial-Associated Membranes-Succinate Mediated Hepatocyte-Macrophage Metabolic Crosstalk in BPAF-Induced Hepatic Insulin Resistance

Xin-yu Hong[1], Ning Wang[1], Jing Leng[1], Da-sheng Lu[1], Jia-le Xu[1], Jing Xu[1], Xiao-qi Yu[1], Ke-lei Qian[1], Zhi-qing Zheng[1], Gong-hua Tao[1], Ping Xiao[1*]

[1]Shanghai Municipal Center for Disease Control and Prevention, Institute of Chemical Safety Evaluation/Key Laboratory of Environmental and Health Impact Assessment of New Pollutants, 1399 at Shenhong Road, Shanghai-200051, China

***Corresponding Author:** Ping Xiao, Shanghai Municipal Center for Disease Control and Prevention, Institute of Chemical Safety Evaluation/Key Laboratory of Environmental and Health Impact Assessment of New Pollutants, 1399 at Shenhong Road, Shanghai-200051, China

Received Date: 20 November 2025; **Accepted Date:** 19 December 2025; **Published Date:** 23 December 2025

Graphical Abstract

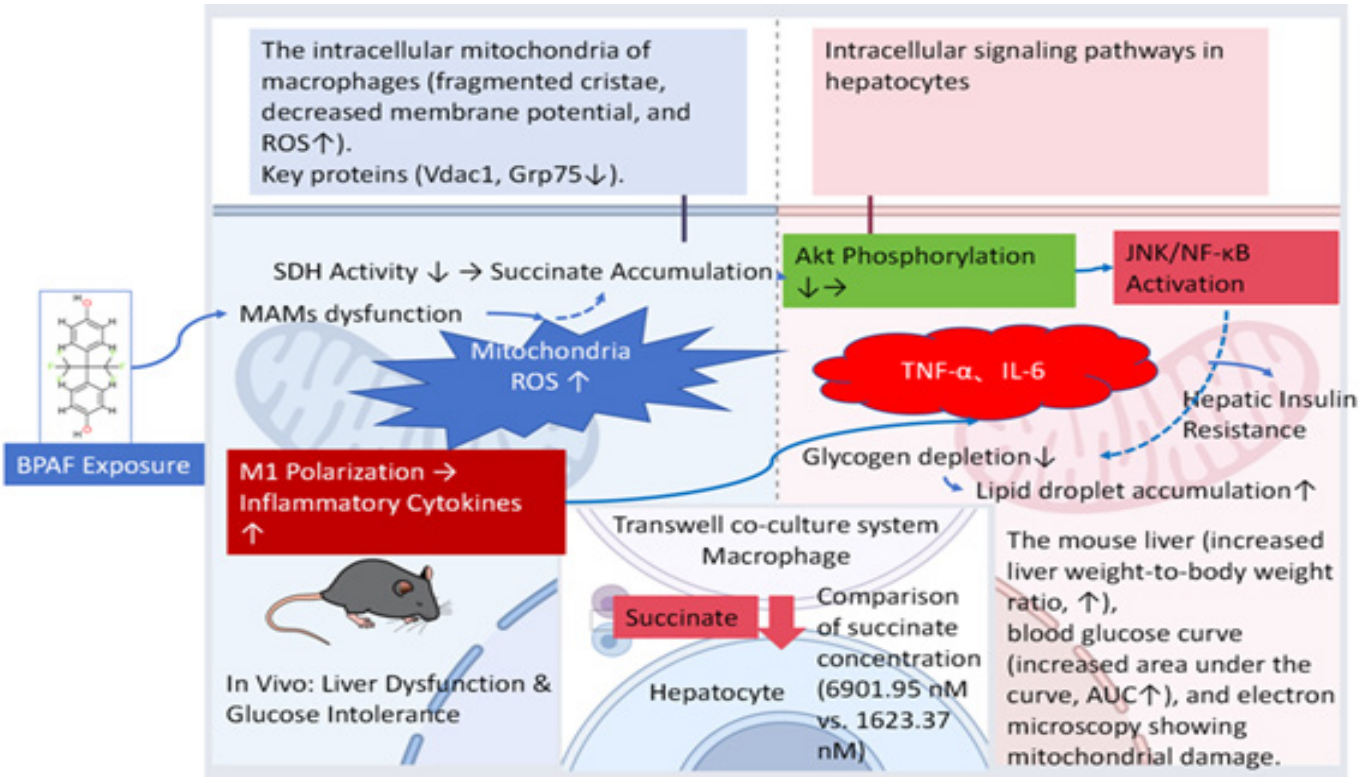

Abstract

Bisphenol AF (BPAF), a widely used Bisphenol A alternative, has an unclear mechanism of hepatic metabolic toxicity. This study explores how BPAF, via mitochondrial-associated membrane (MAMs) dysfunction and succinate accumulation, mediates hepatocyte-macrophage metabolic crosstalk, inducing hepatic insulin resistance. The findings offer a theoretical basis for assessing BPAF's health risks and developing intervention strategies.

Keywords: Bisphenol AF, Mitochondrial-associated membranes, Succinate, Hepatocytes, Macrophages, Insulin resistance

Introduction

Bisphenol AF (BPAF), a fluorinated derivative of bisphenol A (BPA), has emerged as a widely used industrial chemical due to its superior thermal stability and chemical resistance. Structurally, BPAF (IUPAC name: 4,4'-(hexafluoroisopropylidene)diphenol) features two phenolic rings linked by a trifluoromethyl-substituted carbon bridge, rendering it distinct from BPA through the replacement of methyl groups with CF3 moieties [1, 2]. This structural modification enhances its utility as a crosslinking agent in fluoroelastomers, polyimides, and specialty polymers for applications such as electronics, optical fibers, and high-temperature composites [3-5]. Despite its industrial prominence, BPAF's environmental persistence and bioaccumulation potential have raised significant concerns. Studies have detected BPAF in river water (up to 15.3 μg/L), sediments, indoor dust, and even human urine, with exposure routes including ingestion of contaminated food, inhalation of dust, and dermal contact [5, 6].

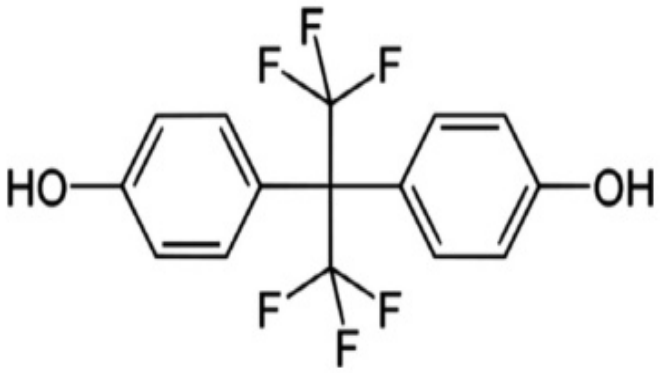

BPAF exhibits potent endocrine-disrupting activity, binding more strongly to estrogen receptors (ERs) than BPA, particularly acting as a full agonist for ERα and an antagonist for Erβ [7, 8]. This interaction disrupts hormonal signaling pathways, contributing to reproductive toxicity, oxidative stress, and metabolic dysregulation. Notably, emerging evidence highlights its hepatotoxic effects. In marine medaka (Oryzias melastigma), BPAF exposure induces hepatic vacuolization, karyopyknosis, and lipid metabolism disruption by altering the expression of genes such as DGAT2, PPARβ, and APOC1, which regulate triglyceride synthesis and lipid transport [8]. Similarly, in zebrafish, BPAF exposure elevates hepatic glucose and glycogen levels, suggesting interference with glucose homeostasis [9]. These findings align with broader observations that BPAF perturbs lipid and carbohydrate metabolism, potentially exacerbating hepatic insulin resistance (IR), a hallmark of metabolic syndrome and type 2 diabetes.

Hepatic IR arises from impaired insulin signaling, often driven by lipid intermediates like diacylglycerols (DAGs) and ceramides, which activate stress kinases such as protein kinase C epsilon (PKCε) and c-Jun N-terminal kinase (JNK). These kinases phosphorylate insulin receptor substrates (IRS), inhibiting downstream Akt activation and glucose uptake [10]. While BPAF's role in modulating these pathways remains underexplored, preliminary data suggest it disrupts insulin-sensitive transcriptional regulators (e.g., FoxO1) and mitochondrial function, exacerbating oxidative stress and inflammation [11]. Furthermore, BPAF exposure in zebrafish embryos downregulates pancreatic β-cell development genes (pdx-1, foxa2), impairing insulin secretion and elevating blood glucose levels [10]. This dual impact on hepatic and pancreatic function underscores its potential to drive systemic metabolic dysfunction.

Despite these advances, the molecular mechanisms linking BPAF exposure to hepatic IR remain poorly defined. Current gaps include the role of BPAF in (1) activating specific lipid-mediated stress kinases, (2) modulating epigenetic regulators of insulin signaling, and (3) disrupting inter-organ crosstalk between the liver and pancreas. This study aims to elucidate these mechanisms, focusing on BPAF-induced perturbations in hepatic lipid metabolism, inflammatory signaling, and insulin receptor transduction pathways. By integrating transcriptomic and metabolomic approaches, we seek to identify novel therapeutic targets to mitigate BPAF-associated metabolic risks.

Materials and Methods

Cell Models: AML12 hepatocytes and RAW264.7 macrophages were employed to evaluate the effects of BPAF on glycolipid metabolism, insulin signaling, mitochondrial function, MAMs structure, and succinate secretion. A Transwell co-culture system was used to simulate metabolic crosstalk

between hepatocytes and macrophages.

The RAW264.7 macrophage cells (SCSP-5036, Chinese Academy of Sciences Cell Bank, Shanghai, China) were cultured in RPMI 1640 medium (Gibco, Thermofisher) containing 10% fetal bovine serum (FBS, Gibco, Australia) at 37℃ with 5% CO_2. The normal mouse hepatocyte AML12 cells (GNM42, Chinese Academy of Sciences Cell Bank, Shanghai, China) were cultured in DMEM/F12 (Gibco, Thermofisher) containing 10% fetal bovine serum (FBS, Gibco, Australia) in a cell culture incubator at 37℃ and 5% CO_2.

Macrophages were seeded into the upper chamber of a Transwell insert, with an appropriate amount of culture medium added to maintain cell growth. The cells were divided into four groups: control group, BPAF treatment groups (100 nM, 500 nM, and 2500 nM). The AML12 hepatocytes were seeded into the lower chamber, with an appropriate amount of culture medium added as well.

A pore size of 3 μm was chosen for the Transwell insert, which allows larger molecules or cell debris to pass through while still restricting the free migration of cells.

After 48 hours of co-culture, AML12 cells were stained with crystal violet and photographed using an inverted microscope (Moticam, ProS5 Plus, China). At the end of the co-culture, the upper chamber of the Transwell insert was carefully removed to avoid disturbing the cells and culture medium in the lower chamber. The collected culture medium was then aliquoted into multiple centrifuge tubes for subsequent metabolic analysis (such as detection of secreted factors and metabolites).

Cell Viability Assay

Cell viability was assessed using the CCK-8 assay kit (Beyotime, Shanghai, China). Cells were seeded in 96-well plates at a density of 3×10^3 cells per well. After treatment, CCK-8 reagent was added, and the cells were incubated at 37°C with 5% CO_2 for 2 hours. The optical density (OD) was measured at 450 nm.

Glycogen Content Determination

The collected AML12 cell pellets were resuspended in an appropriate volume of lysis buffer (e.g., PBS containing protease and phosphatase inhibitors). Cells were lysed by sonication or repeated freeze-thaw cycles to ensure complete lysis. The lysate was centrifuged (12,000 rpm, 10 minutes), and the supernatant was collected for subsequent analysis. An appropriate volume of cell lysate (e.g., 100 μL) was mixed with an equal volume of 6 M HCl and thoroughly mixed. The samples were then heated in a water bath (100°C, 1 hour) to hydrolyze glycogen in the cells to glucose. After cooling, the acidic solution was neutralized with an alkali (e.g., 6 M NaOH) to bring the pH close to neutral. Anthrone was dissolved in concentrated sulfuric acid, typically preparing a 0.2% anthrone solution. An appropriate volume of hydrolyzed sample (e.g., 100 μL) was added to a test tube containing anthrone reagent (e.g., 4 mL). After thorough mixing, the test tube was placed in an ice bath to cool, avoiding uneven color changes due to rapid reactions. The absorbance of the reacted samples was measured at 620 nm using a microplate reader (Tecan, SPARK30086376, Austria). The glucose content in the samples was calculated based on a standard curve, and the glycogen content was then determined based on the hydrolysis ratio of glycogen to glucose (the molecular weight of glycogen is approximately 10 times that of glucose).

AML12 cells were prepared as smears or cultured on coverslips and fixed with 4% paraformaldehyde for 15 minutes. The cells were washed with PBS to remove residual fixative. The cells were treated with 0.5% periodic acid solution (room temperature, 10 minutes) to oxidize the vicinal diols in glycogen to aldehydes. The cells were washed with distilled water to remove the periodic acid. The cells were then immersed in Schiff's reagent and stained at room temperature for 30 minutes. The cells were washed with distilled water to remove unbound Schiff's reagent. The cells were observed under an optical microscope (Leica DM3000, Germany), where glycogen granules appeared magenta.

Lipid Droplet Detection (Nile Red)

AML12 cells were prepared as smears or cultured on coverslips and fixed with 4% paraformaldehyde for 15 minutes. The cells were washed with PBS to remove residual fixative. Subsequently, the cells were stained with 0.1% Nile Red solution (dissolved in ethanol) at room temperature for 15 minutes to label intracellular lipid droplets. Nile Red is a fluorescent dye that specifically binds to lipid droplets and emits red fluorescence. After staining, the cells were washed three times with PBS to remove unbound Nile Red. Finally, the cells were observed under a fluorescence microscope (Leica DM3000, Germany), where lipid droplets appeared as bright red fluorescence in the red fluorescence channel.

Succinate Metabolism Detection

The concentration of succinate in the cell culture supernatant was measured using a Succinate Detection Kit (colorimetric, Abcam, USA). The activity of succinate dehydrogenase (SDH) in RAW264.7 cells was detected using an SDH Assay Kit (Shanghai Enzyme-Linked, China).

Mitochondrial Function Analysis

Mitochondrial membrane potential was determined using TMRE and Rhodamine 123 staining (Beyotime, Shanghai, China). Mitochondrial ATP generation was detected using the mitochondrial ATP fluorescent probe pCMV-Mito-AT1.03 (Beyotime, Shanghai, China). After transfection with the mitochondrial ATP probe, cells were incubated at 37°C with 5% CO_2 for 5 hours. Fluorescent signals were detected using a fluorescence microscope (Leica DM3000, Germany).

Inflammation and Oxidative Stress Detection

Inflammatory cytokines (TNF-α, IL-1β, IL-6) in the cell culture supernatant were detected using ELISA kits (Beyotime, Shanghai, China). Intracellular ROS levels were measured using the DCFH-DA probe (MedChemExpress, USA). The level of MDA was detected using an MDA Assay Kit (Beyotime, Shanghai, China).

Real-Time Quantitative PCR

AML12 cells from the lower chamber were detached from the culture dish using trypsin (Trypsin) or a cell scraper. The detached cells were suspended in an appropriate volume of culture medium and collected by centrifugation (typically at 1000 rpm for 5 minutes). The cell pellet was washed with PBS (phosphate-buffered saline) to remove residual culture medium and trypsin. The cells were collected again by centrifugation for subsequent gene and protein analysis. Total RNA was extracted from tissues or cells using TRIzol (Tiangen, Beijing, China) and reverse-transcribed into cDNA using the FastKing One-Step RT-PCR Kit (Tiangen, Beijing, China). Real-time quantitative PCR (qRT-PCR) was performed on an Mx3000P Real-Time PCR System (Jiatai, Shanghai, China) using SuperReal PreMix Plus (SYBR Green, Tiangen, Beijing, China). Specific primers for the target genes are listed in Table 1. The relative expression of mRNAs was normalized to β-actin.

Gene name	Forward Primer	Reverse Primer
Insr	AGATGAGAGGTGCAGTGTGGCT	GGTTCCTTTGGCTCTTGCCACA
Irs1	TGTCACCCAGTGGTAGTTGCTC	CTCTCAACAGGAGGTTTGGCATG
Irs2	CCAGTAAACGGAGGTGGCTACA	CCATAGACAGCTTGGAGCCACA
Akt	GGACTACTTGCACTCCGAGAAG	CATAGTGGCACCGTCCTTGATC
Gsk3b	GAGCCACTGATTACACGTCCAG	CCAACTGATCCACACCACTGTC
JNK	CGCCTTATGTGGTGACTCGCTA	TCCTGGAAAGAGGATTTTGTGGC
β-actin	CATTGCTGACAGGATGCAGAAGG	TGCTGGAAGGTGGACAGTGAGG

Table1: List of Primers for Quantitative Real-Time Polymerase Chain Reaction (qRT-PCR)

Western Blot Analysis

Total proteins were extracted from tissues or cells using lysis buffer (Thermo Fisher, USA). Protein concentrations were quantified using a BCA Protein Assay Kit (Beyotime, Shanghai, China). Denatured proteins were separated by SDS-PAGE and then transferred to PVDF membranes (Millipore, USA) by electroblotting. After blocking with 5% skim milk at room temperature for 1 hour, the membranes were incubated with primary antibodies against Akt1, Gsk3b, JNK1/MAPK8, and NF-κB p65 (Beyotime, Shanghai, China) at 4℃ overnight. The membranes were then incubated with diluted secondary antibodies (1:1000, Beyotime, Shanghai, China). Band intensities were quantified using ImageJ software.

Metabolomics Analysis

Cells were divided into four groups: the control group and the BPAF treatment group (2500 nM). After 48 hours of BPAF exposure, the original culture medium was removed, and each culture flask was washed three times with 1 mL of ammonium acetate solution (150 mmol/L). Intracellular metabolites were extracted using a methanol/chloroform/water extraction solvent (8:1:1, v/v/v). The extracted solution was sonicated on ice for 10 minutes, followed by homogenization (60 s) and centrifugation (12000 rpm, 5 min, 4°C). The supernatant was further sonicated on ice and centrifuged again. Subsequently, the supernatant was dried under a nitrogen stream and resuspended in a mixture of acetonitrile/water (9:1, v/v). The solvent volume was adjusted according to the cell count results of each group to ensure consistent metabolite quantities for loading. The solution was sonicated and centrifuged again, then filtered through a 0.22 μm membrane for UPLC-MS analysis.

Non-targeted metabolomics analysis was performed using a UPLC system coupled with a Q Exactive mass spectrometer (Agilent, 5975C, USA). A total of 5 μL of metabolite sample was injected into the UPLC-MS system using a BEH HILIC column (2.1×100 mm, 1.7 μm) maintained at 35°C.

Total Metabolite Analysis

For total metabolites, the relative standard deviation (RSD) of chromatographic peaks ranged from 1% to 26%, demonstrating high stability and precision of our analytical method. Biochemical structures were confirmed through library matching (LipidMaps, ChEBI, KEGG, and PubChem) and verification with standard reference materials. Finally, duplicates and blanks were excluded to generate data files for statistical analysis [12, 13].

Differential Metabolites (DMs) Identification and Metabolic Pathway Analysis

Metabolite signal data were log-transformed and expressed as mean ± SD. After assessing normality (Kolmogorov-Smirnov test) and homogeneity of variance (Levene's test), t-tests or Wilcoxon rank-sum tests were performed to evaluate the significance of differences between the BPAF treatment group (2500nM) and the control group (0 nM) us-

ing R (version 4.2.2). Pearson or Spearman tests were applied to assess the significance of differences across all concentrations. Subsequently, partial least squares-discriminant analysis (PLS-DA) was generated, and variable importance in projection (VIP) values were calculated using R. Differential metabolites (DMs) were selected based on significance test p-values < 0.05 and VIP values > 1.0. Volcano and Venn diagrams illustrating upregulated and downregulated DMs in each treatment group were created using GraphPad Prism (version 10.4.0) and R. Additionally, the signal data of DMs were submitted to MetaboAnalyst 5.0 (http://www.metaboanalyst.ca) for metabolite set enrichment analysis to determine the chemical structure classification of DMs and pathway analysis to identify enriched metabolic pathways. Pie charts illustrating DM classification were generated using GraphPad Prism. Enrichment p-values and pathway impact values were calculated based on pathway analysis. To include more metabolic pathways for further analysis, all major affected pathways across concentrations were screened based on enrichment p-values < 0.1 and pathway impact values > 0.1, with some pathways having p-values < 0.05 but lower pathway impact values. Key DMs were selected as metabolites enriched in these metabolic pathways [14]. Hierarchical clustering analysis to illustrate the expression patterns of DMs was performed using the ComplexHeatmap R package. Metabolic pathways were drawn with reference to KEGG (http://www.genome.jp/kegg/).

Animal Model: C57BL/6J mice were orally gavaged with BPAF for 90 days to assess hepatic metabolism, inflammation, and insulin sensitivity.

Animal Housing and Administration

Six-week-old male C57BL/6J mice, weighing 21–23 g, of specific pathogen-free (SPF) grade were obtained from Zhejiang Vitonliva Biotechnology Co., Ltd. (Hangzhou, Zhejiang Province, China). After a 1-week acclimatization period, the mice were randomly assigned to four groups (vehicle control group, BPAF-0.5, 4, 32 mg/kg), with six animals per group. All animals received oral gavage of BPAF corn oil solution (0, 0.1, 0.8, 6.4 mg/mL) at a dosage of 5 mL/kg body weight once daily. On day 90, the mice from each group were sacrificed, and blood and liver tissues were collected for subsequent evaluation. This study was approved by the Animal Ethics Committee of the Shanghai Center for Disease Control and Prevention and conducted in accordance with the National Institutes of Health Guide for the Care and Use of Laboratory Animals.

Body Weight Measurement

Body weights were measured once a week during the experimental period.

Liver Weight and Organ Index

At the end of the experiment, all animals were subjected to gross dissection. The absolute weight of the liver was recorded, and the relative weight (liver-to-body weight ratio) was calculated.

Biochemical Blood Tests

Blood glucose levels were measured twice weekly using glucose test strips (glucose dehydrogenase method, Roche, USA). Levels of AST, ALT, ALP, TG, CHOL, D3H, and NEFA were measured using an automated biochemical analyzer (AU680, Beckman Coulter, USA).

Inflammatory cytokine levels in the serum were measured using ELISA: high-sensitivity C-reactive protein (HS-CRP) (latex-enhanced immunoturbidimetric assay, Nanjing Jiancheng, Jiangsu, China), TNF-α, IL-1β, IL-6 (Beyotime, Shanghai, China).

Real-Time Quantitative PCR

Total RNA was extracted from tissues or cells using TRIzol (Tiangen, Beijing, China) and reverse-transcribed into cDNA using the FastKing One-Step RT-PCR Kit (Tiangen, Beijing, China). Real-time quantitative PCR (qRT-PCR) was performed on an Mx3000P Real-Time PCR System (Jiatai, Shanghai, China) using SuperReal PreMix Plus (SYBR Green, Tiangen, Beijing, China). Specific primers for the target genes are listed in Table 1. The relative expression of mRNAs was normalized to β-actin.

Histopathological Analysis (Hematoxylin and Eosin Staining and Oil Red O Staining of Frozen Sections)

Liver tissues from mice with BPAF-induced chronic liver injury were collected and fixed in 4% paraformaldehyde (Senbeiga, Jiangsu, China) overnight. The tissues were then dehydrated in ethanol and embedded in paraffin. Paraffin blocks were sectioned at 5 μm. One set of sections was stained with hematoxylin (Solarbio, Beijing, China) and eosin (Sangon, Shanghai, China) for histopathological evaluation. Another set of sections was stained with Oil Red O using an Oil Red O staining kit (Jiancheng, Nanjing, Jiangsu, China) to detect lipid accumulation. The stained sections were observed and photographed under a light microscope (Leica DM3000, Germany).

Immunofluorescence Staining of Frozen Sections

Liver tissue samples from mice with BPAF-induced chronic liver injury were prepared as frozen sections. Sections were fixed in 4% paraformaldehyde (Senbeiga, Jiangsu, China) at room temperature for 30-60 minutes, washed three times with PBS (5 minutes each), treated with 0.3% Triton X-100 (in PBS) at room temperature for 15 minutes, and washed three times with PBS (5 minutes each). Sections were blocked with immunostaining blocking solution (Beyotime, Shanghai, China) at 37°C for 2 hours (no need to wash). Primary antibody: NF-κB p65 Rabbit Monoclonal Antibody (Beyotime, Shanghai, China) was diluted in immunostaining antibody dilution solution (Beyotime, Shanghai, China). Tissues were circled

with a blocking pen and incubated with a small amount of antibody in a humidified chamber at 4°C overnight. Sections were washed three times with PBS (5 minutes each) and incubated with an anti-rabbit FITC immunofluorescence staining kit (Beyotime, Shanghai, China) in the dark at 37°C for 2 hours. Sections were washed three times with PBS (5 minutes each) and stained with 2 μg/mL DAPI (Sewell, Hubei, China) for nuclei. Sections were washed three times with PBS (5 minutes each) and mounted with an anti-fade mounting medium. For images comparing fluorescence intensity, the acquisition parameters of the fluorescence microscope must be kept consistent, and fluorescence intensity was analyzed using ImageJ software.

Fluorescence Microplate Reader Analysis of M1 and M2 Macrophage Ratios

Single-cell suspensions were isolated from mouse livers. Liver tissues were minced and dissociated using a single-cell suspension instrument (MEDIMACHINE II, Finland). Red blood cells were lysed with RBC lysis buffer to avoid interference with flow cytometry. Cells were fixed and permeabilized to allow antibody entry. For each dose group, 1 mL of cell suspension was mixed with 1 μL F4/80 Rabbit Monoclonal Antibody (Beyotime, Shanghai, China) and 1 μL CD11c Rabbit Monoclonal Antibody (Beyotime, Shanghai, China) for M1 macrophage labeling. Another 1 mL of cell suspension was mixed with 1 μL F4/80 Rabbit Monoclonal Antibody (Beyotime, Shanghai, China) and 1 μL CD206/MRC1 Rabbit Monoclonal Antibody (Beyotime, Shanghai, China) for M2 macrophage labeling. Samples were incubated at 4°C overnight and then incubated with an anti-rabbit FITC immunofluorescence staining kit (Beyotime, Shanghai, China) in the dark at 37°C for 2 hours. After incubation, cells were washed with PBS to remove unbound antibodies. The fluorescence microplate reader (Tecan, SPARK30086376, Austria) was set to the appropriate fluorescence wavelength. Cell suspensions labeled for M1 and M2 macrophages were added to a 96-well plate in triplicate for each concentration, and fluorescence intensity was measured. The ratio of fluorescence intensity between experimental and control groups was compared, and statistical analysis was performed to determine significance.

Transmission Electron Microscopy

Tissue samples were collected and fixed in electron microscopy fixative (Servicebio, Hubei, China) in the dark at room temperature for 2 hours, dehydrated with acetone, and polymerized in an oven at 60°C for 48 hours. Ultrathin sections (60-80 nm) were cut and stained with 2% saturated uranyl acetate solution and 2.6% lead citrate solution. Mitochondrial morphological changes were observed under a transmission electron microscope (HT7700 Exalens, Hitachi, Japan).

Statistical Analysis

Data were analyzed using GraphPad Prism 8 and presented as mean ± standard error (SE). One-way analysis of variance (ANOVA) was used to assess differences among multiple groups, followed by Tukey's HSD test for pairwise comparisons with the control group, with the significance level set at $p < 0.05$.

For Benchmark Dose (BMD) analysis, we followed the guidelines of the United States Environmental Protection Agency (USEPA) and used the e(BMD) model and Benchmark Dose Software (BMDS, version 3.2). The best-fit model was selected based on the lowest Akaike Information Criterion (AIC) to calculate parameters such as BMD, BMDL, and BMDU, which represent the benchmark dose and its 95% confidence interval, respectively. All analyses were conducted using BMD50, corresponding to a 50% increase in the frequency of genotoxicity detection above the background level. Data were grouped by exposure route and analyzed using a joint covariate BMD model to ensure consistency and computational feasibility. The exponential and Hill model families recommended by the European Food Safety Authority (EFSA) for continuous data analysis were applied [15]. Covariate analysis assumed that model parameters for the maximum response and steepness of the dose-response curve remained constant. Unique identifiers were assigned to datasets with different parameters, serving as covariates for background response, potency, and within-group variance. For compounds with multiple datasets, the lowest BMDL value was used for the Margin of Exposure (MOE) calculation.

Results

BPAF's Toxic Effects on Macrophages and Impact on MAMs Function: BPAF significantly inhibited macrophage viability, induced an increase in mitochondrial ROS, and disrupted MAMs coupling.

BPAF Induces Succinate Accumulation and Alters Mitochondrial Function

After 24 hours of BPAF treatment, the OD value of CCK-8 at 5000 nM was significantly downregulated (F values were 0.001133, 0.004967, 0.001933, 0.01060, and 0.01560; P values were 0.9997, 0.7896, 0.9942, 0.1987, and 0.0376, respectively). After 48 hours of BPAF treatment, the OD values of CCK-8 at 500, 2500, and 5000 nM were significantly downregulated (F values were 0.02147, 0.01567, 0.08743, 0.09040, and 0.1063; P values were 0.7244, 0.8903, 0.0036, 0.0028, and 0.0008, respectively). After 72 hours of BPAF treatment, the OD values of CCK-8 at 2500 and 5000 nM were significantly downregulated (F values were -0.03083, 0.04077, 0.1577, 0.2975, and 0.3818; P values were 0.9902, 0.9681, 0.1705, 0.0060, and 0.0009, respectively). Therefore, the concentrations of 0, 100, 500, and 2500 nM were selected for 24-hour BPAF treatment (Figure 1A).

After 24 hours of BPAF treatment, the concentration of succinate in the culture supernatant of RAW264.7 cells at 5000 nM was significantly increased (F values were -356.7, -1417,

and -2800; P values were 0.8500, 0.0750, and 0.0023, respectively) (Figure 1B).

After 24 hours of BPAF treatment, the fluorescence signals of mitochondrial membrane potential (TMRE) and (Rhodamine 123) gradually weakened with increasing BPAF concentration, and the fluorescence signal of mitochondrial ATP (pC-MV-Mito-AT1.03) also gradually weakened with increasing BPAF concentration (Figure 1C).

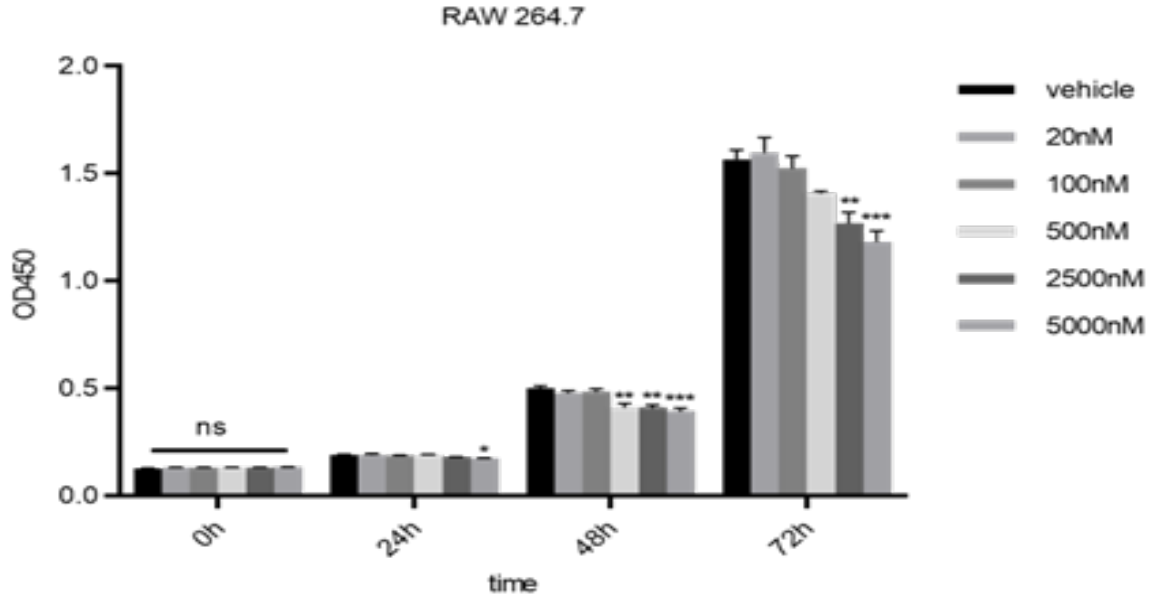

Figure1A: CCK-8 OD values of RAW264.7 macrophages after 24 hours of BPAF treatment

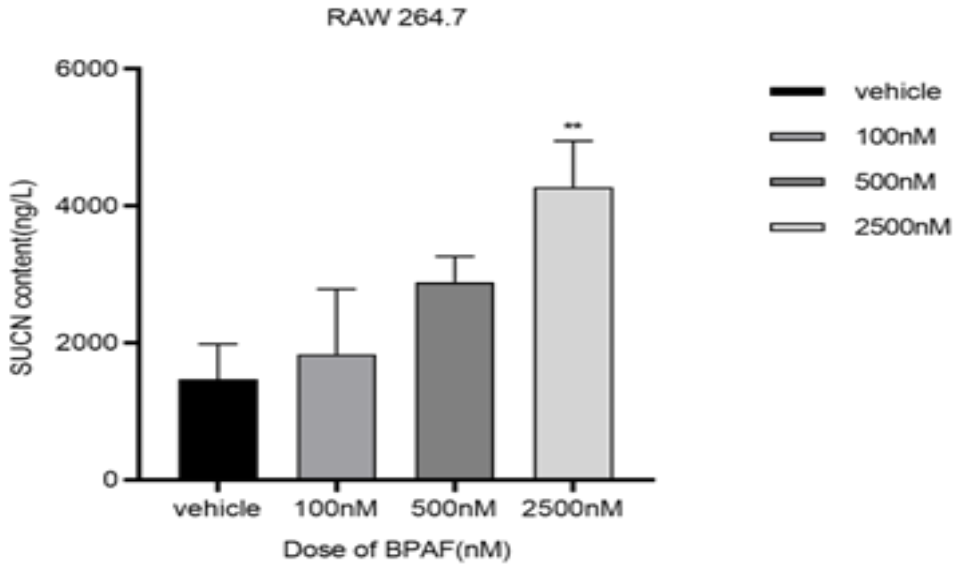

Figure1B: Concentration of succinate in the culture supernatant of RAW264.7 cells after 24 hours of BPAF treatment

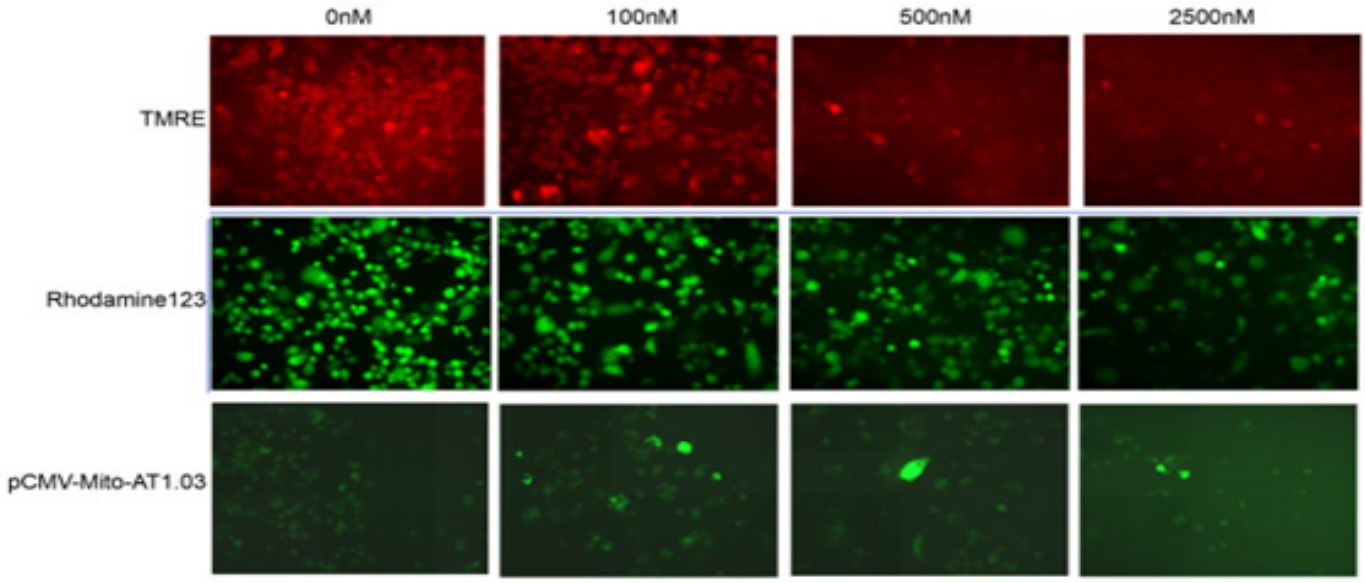

Figure1C: Mitochondrial membrane potential (TMRE, Rhodamine 123) and mitochondrial ATP fluorescent probe (pCMV-Mito-AT1.03) after 24 hours of BPAF treatment

The data represent the mean results of three independent experiments (mean ± SD).
(*: Compared with the negative control group, P < 0.05;
**: Compared with the negative control group, P < 0.01;
***: Compared with the negative control group, P < 0.001;
****: Compared with the negative control group, P < 0.0001)

Figure1: Effects of BPAF on succinate accumulation and mitochondrial function.

BPAF Induces Inflammatory Cytokine Production and Oxidative Stress

After 24 hours of BPAF treatment, the levels of TNF-α in the culture supernatant of RAW264.7 cells at 100, 500, and 2500 nM were significantly increased (F values were -7.625, -10.10, and -12.56; P values were 0.0050, 0.0009, and 0.0002, respectively). The levels of IL-6 in the culture supernatant of RAW264.7 cells at 100, 500, and 2500 nM were significantly increased (F values were -64.62, -71.82, -75.28; P values were <0.0001, <0.0001, <0.0001, respectively). The level of IL-1β in the culture supernatant of RAW264.7 cells at 2500 nM was significantly increased (F values were 0.02811, 0.6988, -6.462; P values were >0.9999, 0.6588, <0.0001, respectively) (Figure 2A).

After 24 hours of BPAF treatment, the fluorescence signal of the DCFH-DA probe significantly increased with increasing BPAF concentration compared to the negative control group (Figure 2B).

After 24 hours of BPAF treatment, the levels of MDA in the culture supernatant of RAW264.7 cells at 500 and 2500 nM were significantly increased (F values were -1105, -22383, -31595; P values were 0.1088, <0.0001, <0.0001, respectively) (Figure 2C).

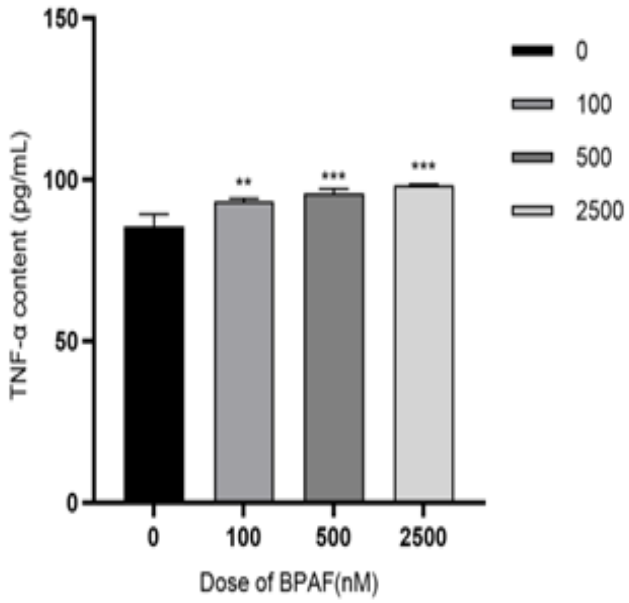

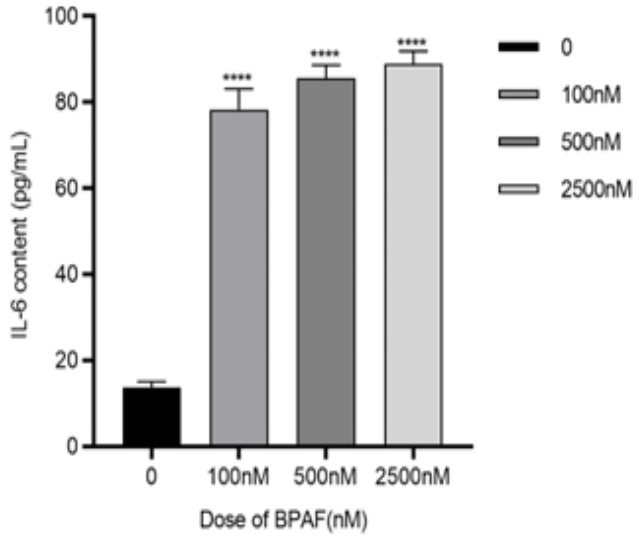

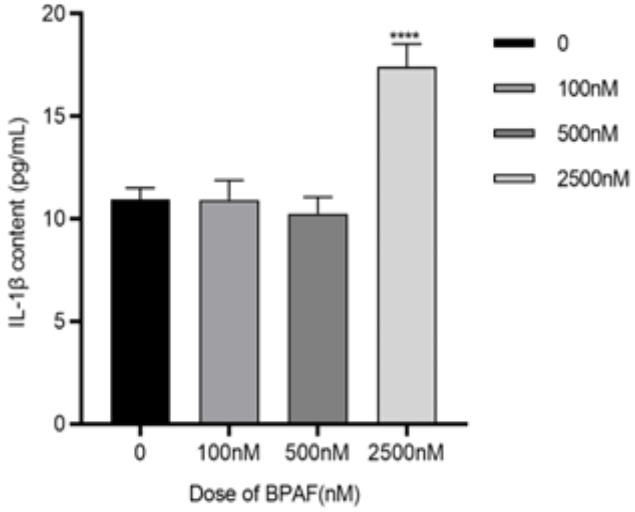

Figure2A: Levels of TNF-α, IL-6, and IL-1β in the culture supernatant of RAW264.7 cells after 24 hours of BPAF treatment

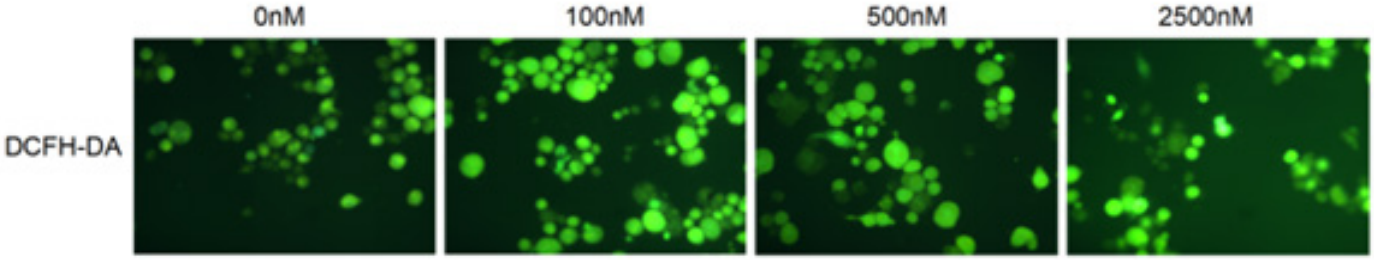

Figure2B: DCFH-DA fluorescence probe in RAW264.7 cells after 24 hours of BPAF treatment

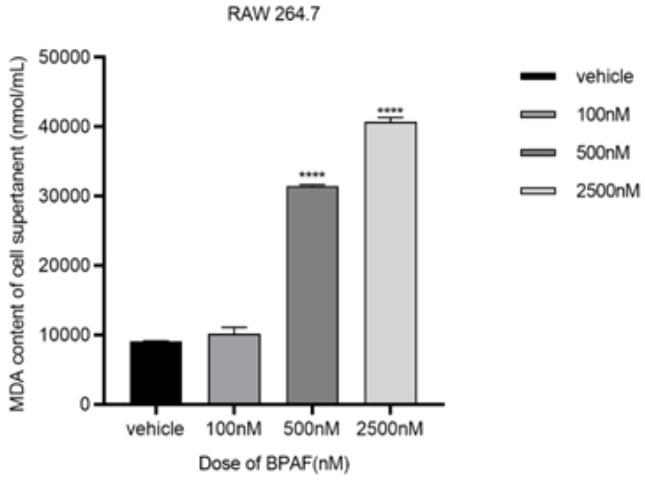

Figure2C: Levels of MDA in the culture supernatant of RAW264.7 cells after 24 hours of BPAF treatment.

The data represent the mean results of three independent experiments (mean ± SD).
(*: Compared with the negative control group, P < 0.05;
**: Compared with the negative control group, P < 0.01;
***: Compared with the negative control group, P < 0.001;
****: Compared with the negative control group, P < 0.0001)

Figure2: Effects of BPAF on the production of inflammatory cytokines and oxidative stress.

Changes in Succinate Secretion: In the Transwell co-culture system, the concentration of succinate in the supernatant of hepatocytes treated with BPAF was significantly elevated.

BPAF Induces Succinate Metabolic Reprogramming in Macrophages

Using the Transwell co-culture model, it was found that BPAF exposure (100–2500 nM) significantly increased the succinate concentration in the supernatant of RAW264.7 macrophages (BMD = 6901.95 nM, BMDL = 1623.37 nM) in a dose-dependent manner (Figure 1). Concurrently, suc-

cinate dehydrogenase (SDH) activity in the BPAF-treated group decreased by 37.6% compared to the control group (500 nM treatment, $p < 0.01$), suggesting that BPAF induces succinate accumulation by inhibiting SDH activity (Figure 3).

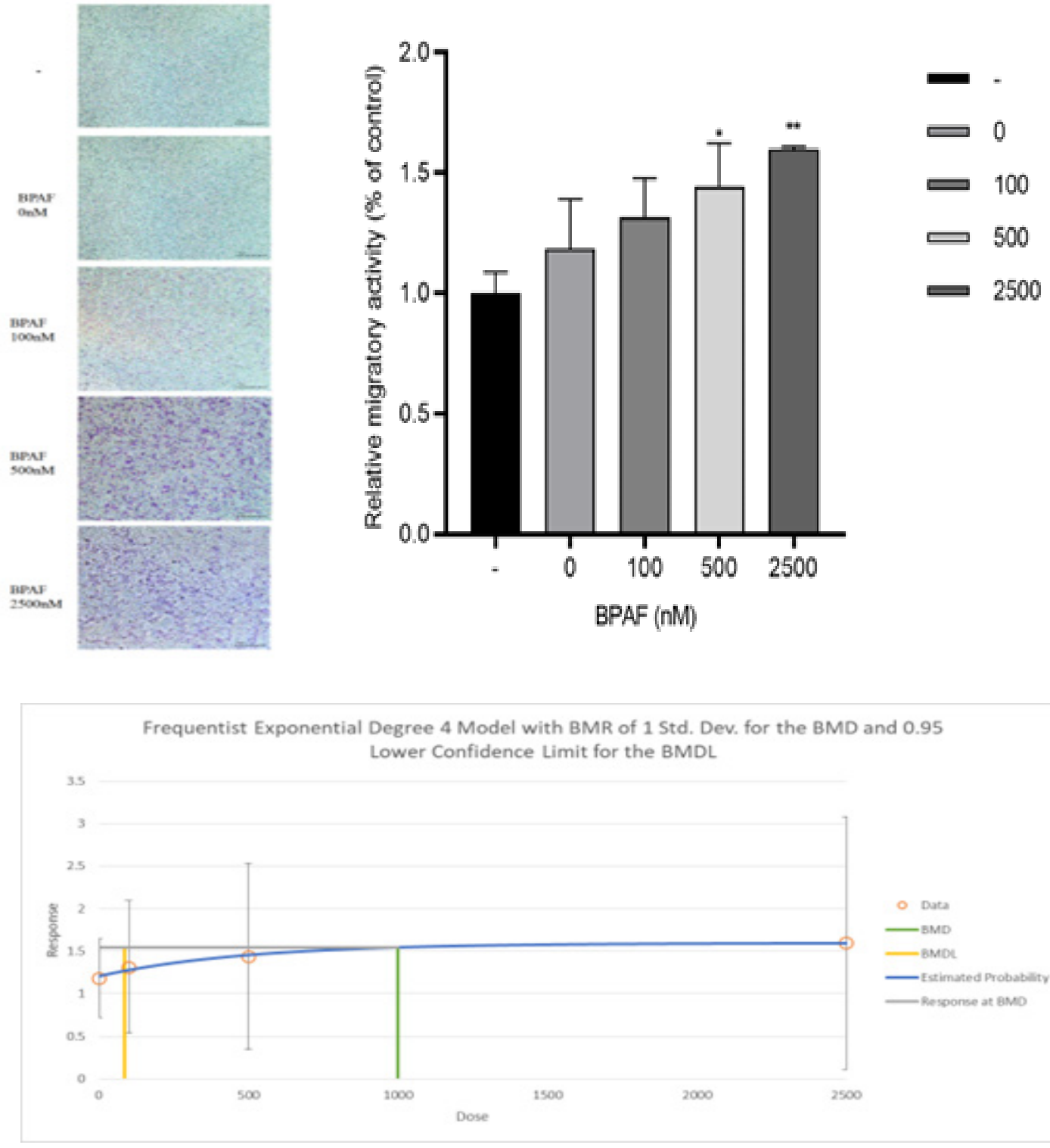

Figure3A: Crystal violet staining and relative migration rate of AML12 cells in the lower chamber of the Transwell system after 48 hours of BPAF treatment

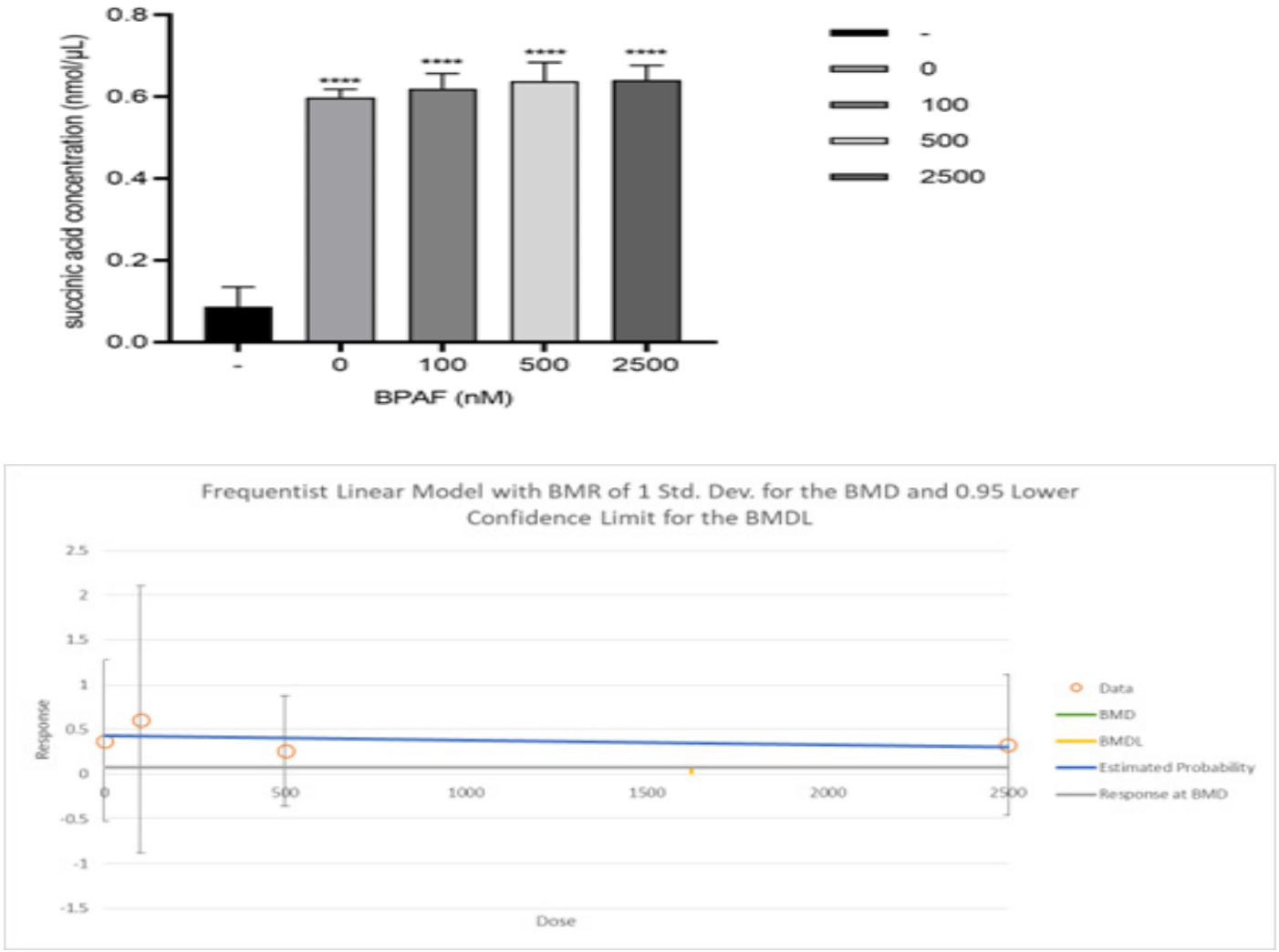

Figure3B: Succinate concentration in the supernatant of AML12 cells in the lower chamber of the Transwell system after 48 hours of BPAF treatment

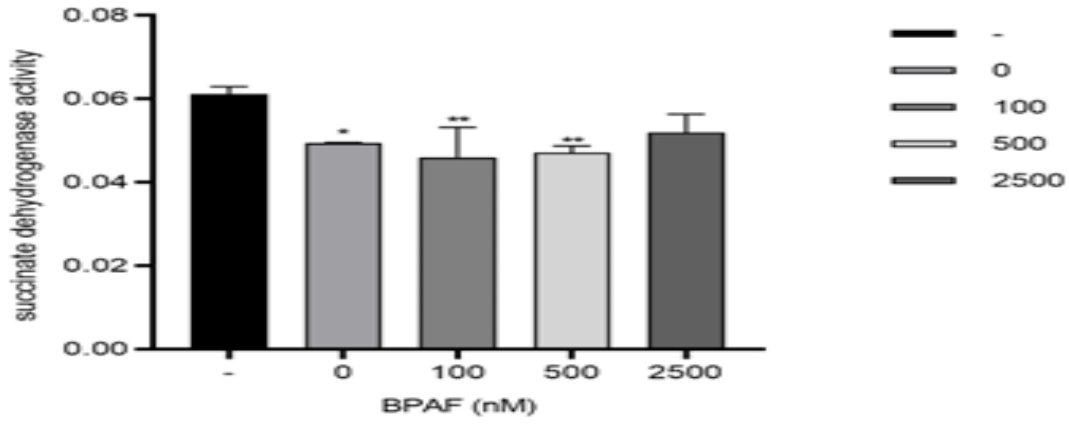

Figure3C: Succinate dehydrogenase activity in the supernatant of AML12 cells in the lower chamber of the Transwell system after 48 hours of BPAF treatment

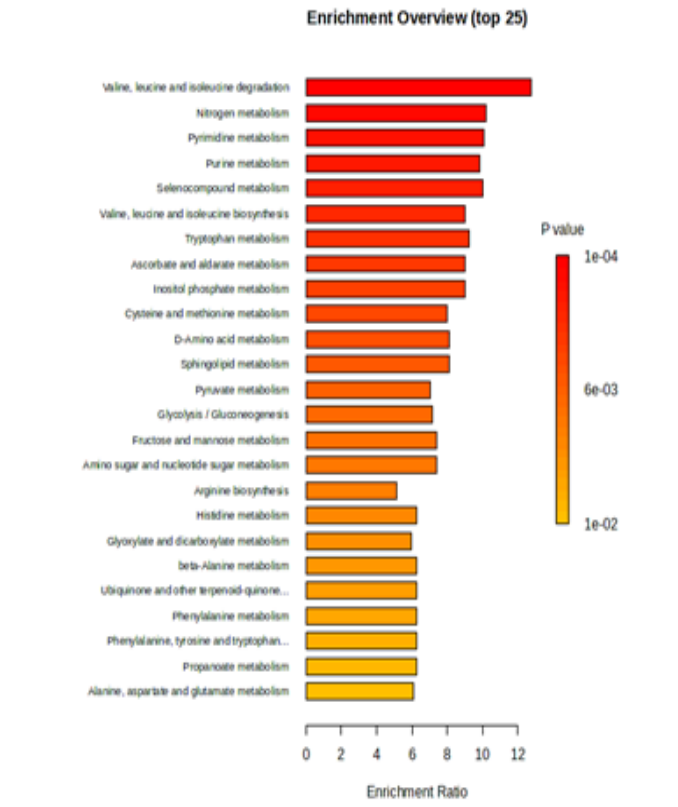

Figure3D: Amino acid metabolomics enrichment analysis of AML12 cells after 48 hours of BPAF treatment

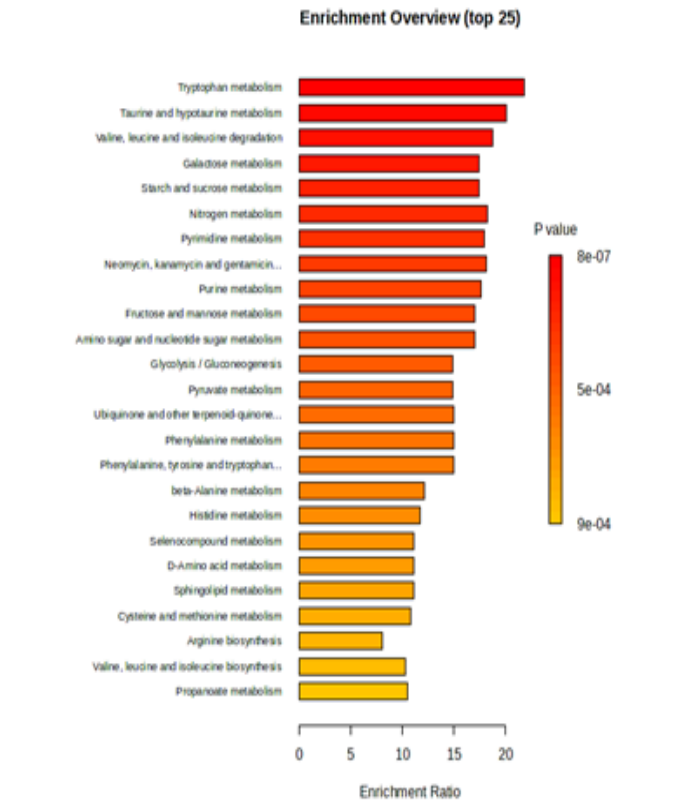

Figure3E: HILIC metabolomics enrichment analysis of AML12 cells after 48 hours of BPAF treatment

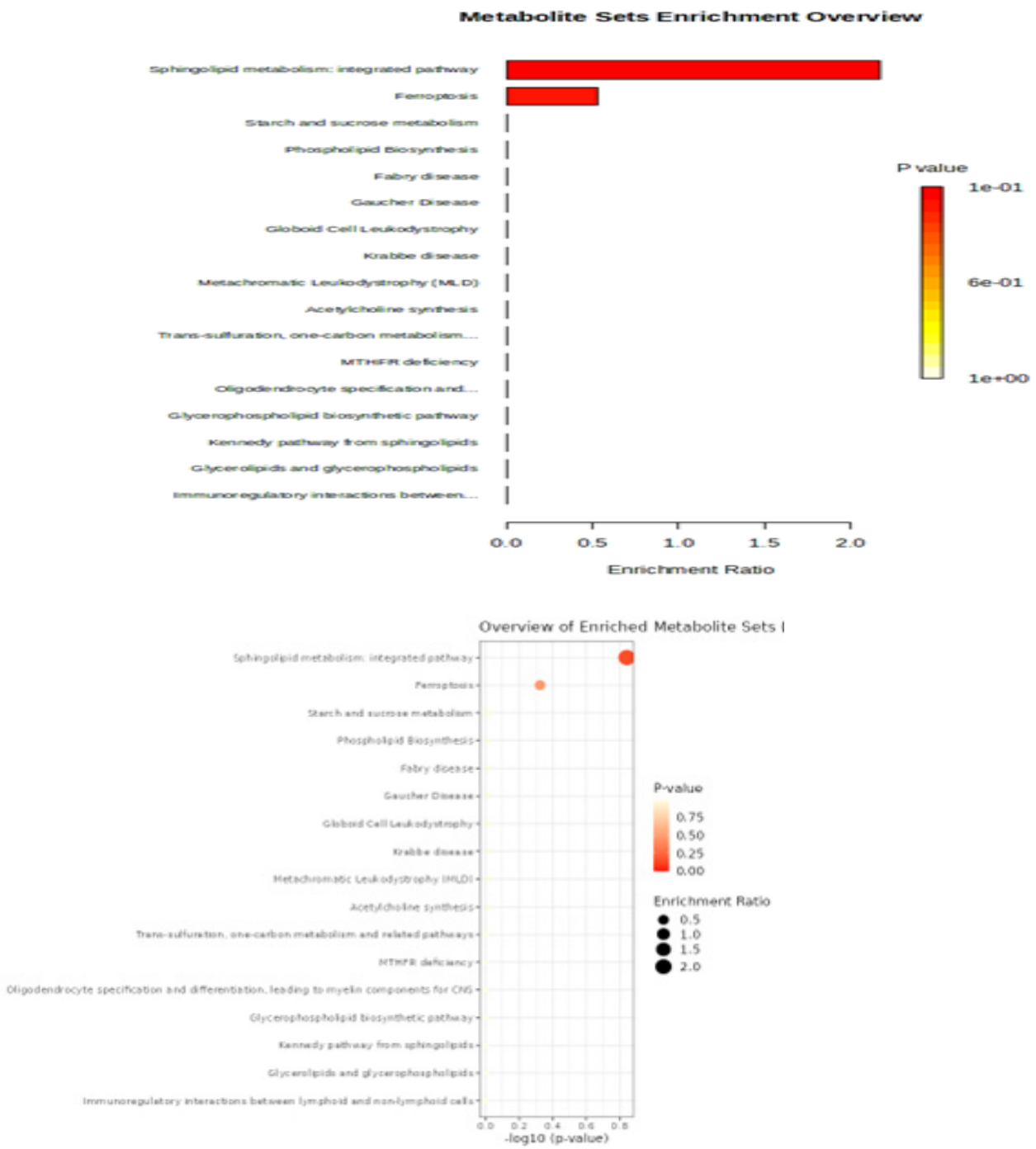

Figure3F: Lipid metabolomics enrichment analysis of AML12 cells after 48 hours of BPAF treatment

The data represent the mean results of three independent experiments (mean ± SD).
(*: Compared with the negative control group, P < 0.05;
**: Compared with the negative control group, P < 0.01;
***: Compared with the negative control group, P < 0.001;
****: Compared with the negative control group, P < 0.0001))

Figure3: BPAF induces succinate metabolic reprogramming in macrophages.

Inhibition of Insulin Signaling Pathway: BPAF caused abnormal glycolipid metabolism in hepatocytes, reduced the phosphorylation level of Akt, and upregulated JNK activity. The Sucnr1 receptor played a regulatory role in this process.

BPAF Induces Abnormal Glycolipid Metabolism in Hepatocytes

The anthrone method revealed that glycogen content in AML12 hepatocytes increased 1.8-fold compared to the control group after BPAF exposure (2500 nM treatment, $p < 0.001$). PAS staining further confirmed a significant increase in glycogen granules within the hepatocyte cytoplasm (increased density of magenta granules, see Figure 4). The abnormal accumulation of glycogen is closely related to the dysregulation of the insulin signaling pathway. Additionally, after 24 hours of BPAF treatment in AML12 mouse hepatocytes, the red fluorescence intensity of lipid droplet detection (Nile Red) in AML12 cells significantly increased with the dose escalation. The fluorescence intensity reached the highest levels in the 500 nM and 2500 nM dose groups, as shown in Figure 4.

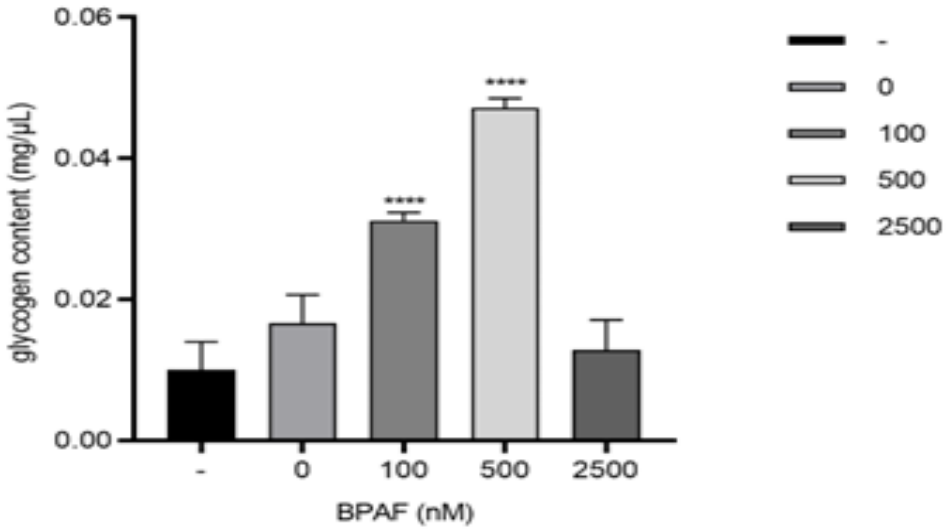

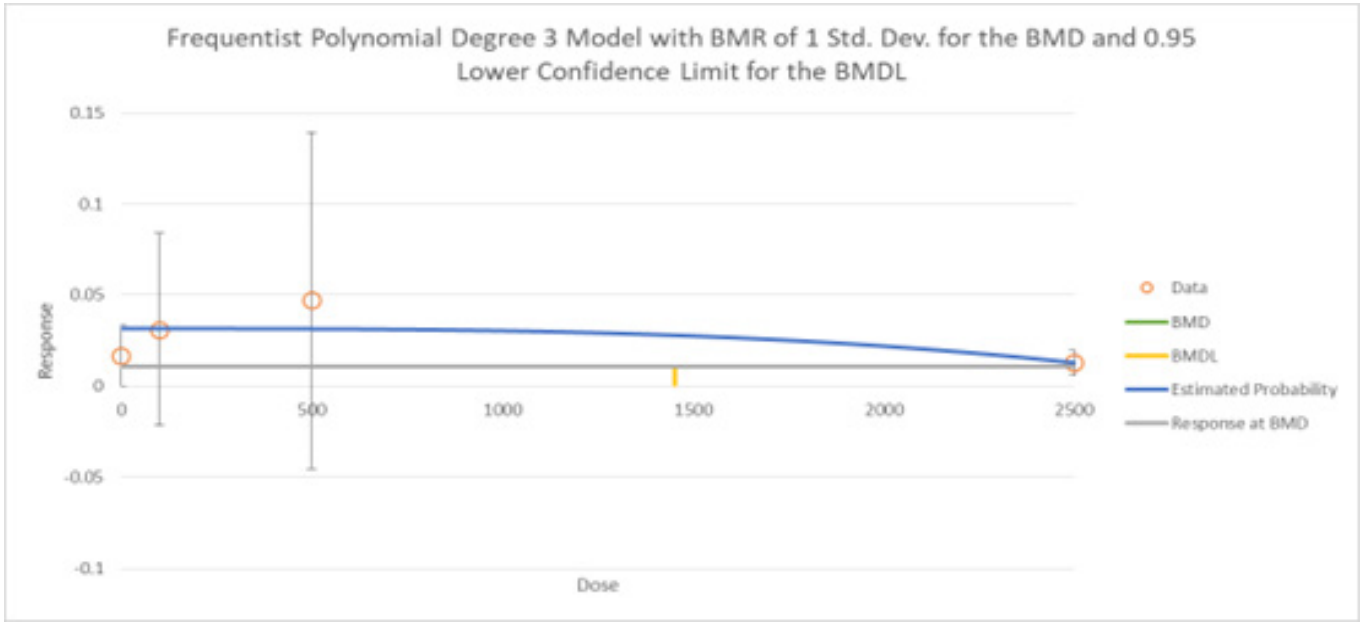

Figure4A: Glycogen content in AML12 cells in the lower chamber of the Transwell system after 48 hours of BPAF treatment (detected by the anthrone method)

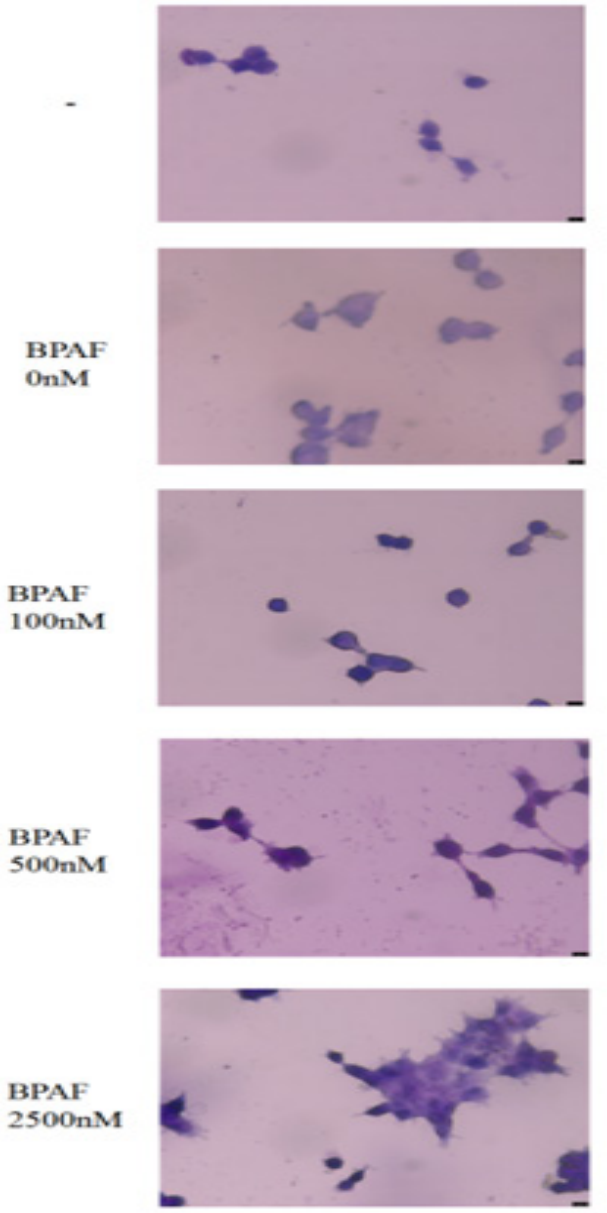

Figure4B: Glycogen content in AML12 cells in the lower chamber of the Transwell system after 48 hours of BPAF treatment (PAS staining)

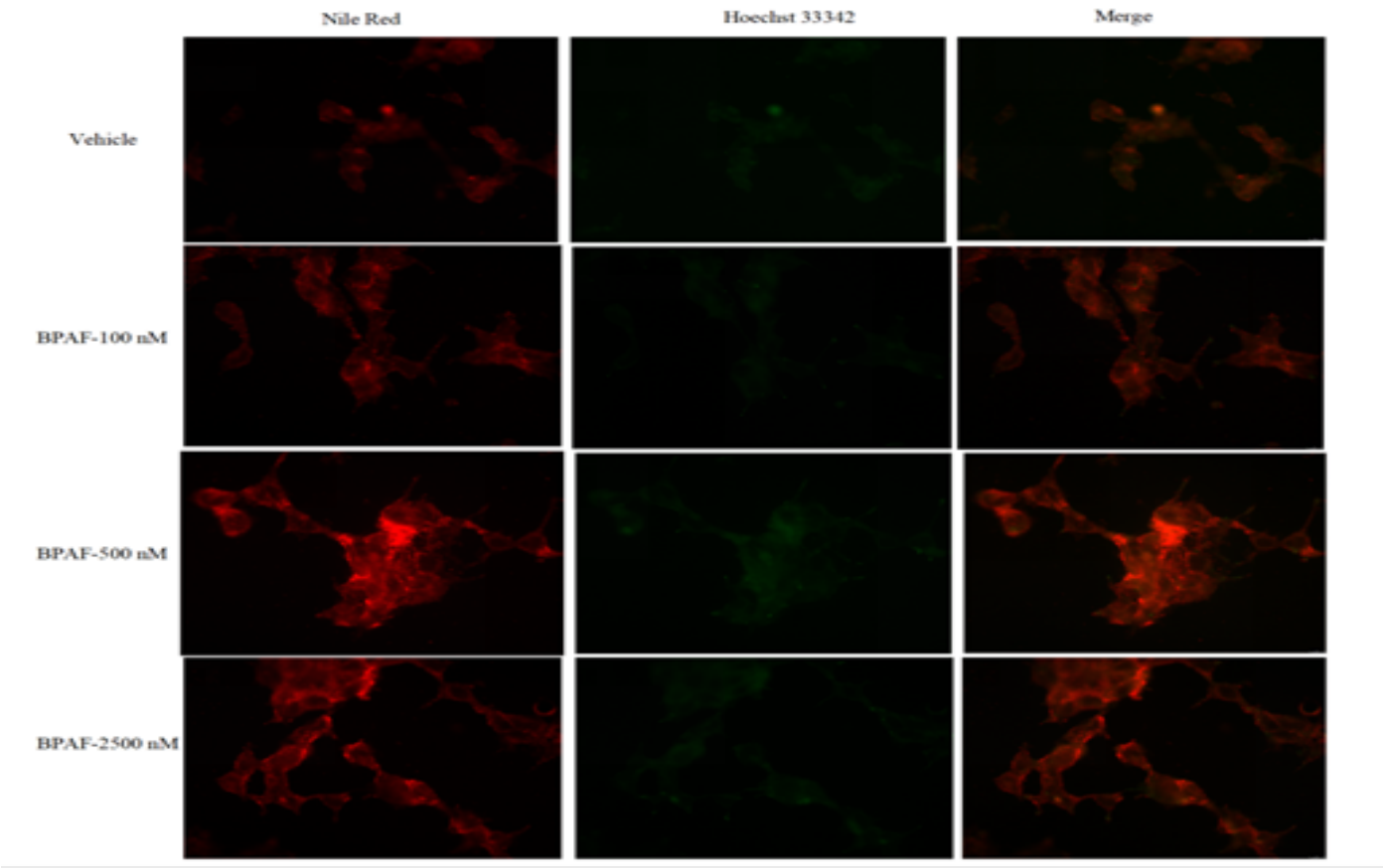

Figure4C: Lipid droplet detection in AML12 cells in the lower chamber of the Transwell system after 48 hours of BPAF treatment (Nile Red staining)

The data represent the mean results of three independent experiments (mean ± SD).
(*: Compared with the negative control group, P < 0.05;
**: Compared with the negative control group, P < 0.01;
***: Compared with the negative control group, P < 0.001;
****: Compared with the negative control group, P < 0.0001)

Figure4: BPAF induces glycogen metabolic disorder in hepatocytes.

BPAF Suppresses the Expression of Key Molecules in the Insulin Signaling Pathway

qRT-PCR results showed that BPAF significantly downregulated the mRNA expression of insulin receptor (Insr), insulin receptor substrate 1/2 (Irs1/2), and Akt in AML12 cells (BMD range: 988.67–2522.67 nM), with the most significant inhibition of Irs2 expression (BMD = 988.67 nM, BMDL = 626.36 nM) (Figure 3). Western blot analysis further confirmed that the protein levels of Akt1 (BMD = 874.26 nM) and Gsk3b (BMD = 2345.27 nM) in the BPAF-treated group decreased by 58% and 42%, respectively (p < 0.001), indicating inactivation of the insulin signaling pathway (Figure 5).

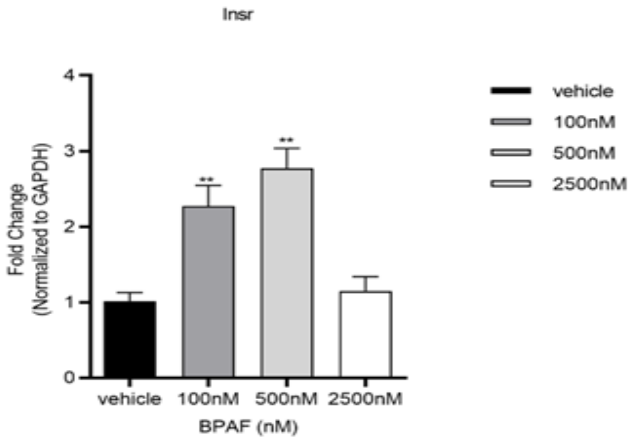

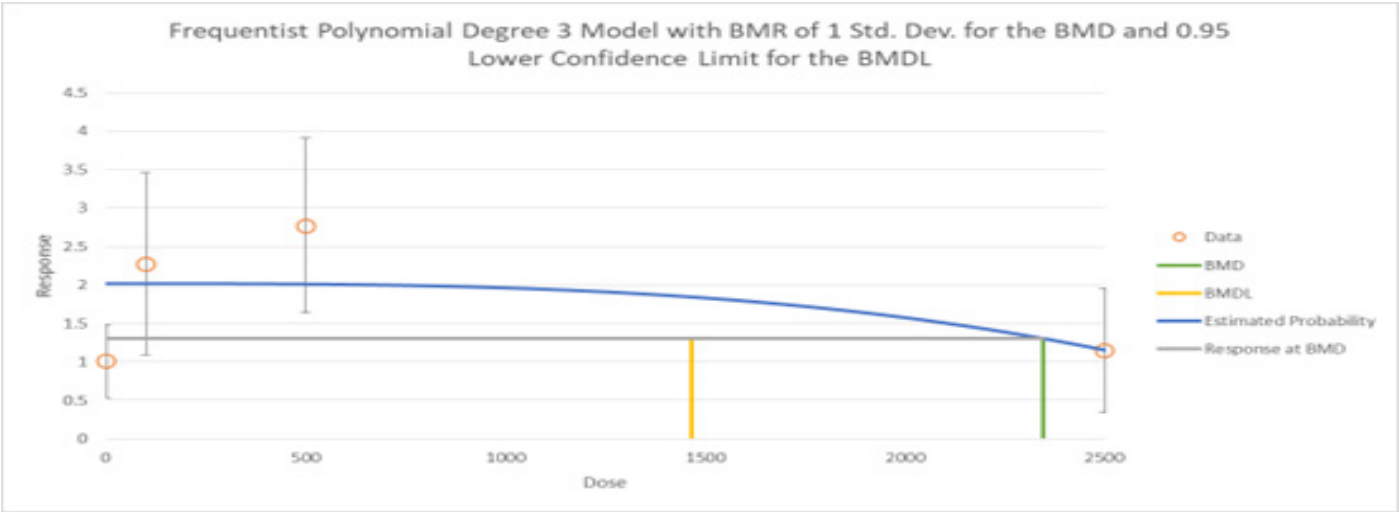

Figure5A: Expression of the Insr gene in AML12 cells in the lower chamber of the Transwell system after 48 hours of BPAF treatment

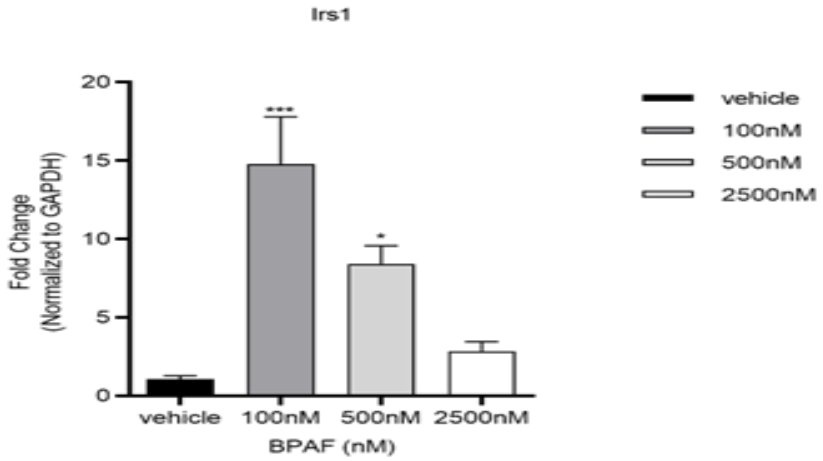

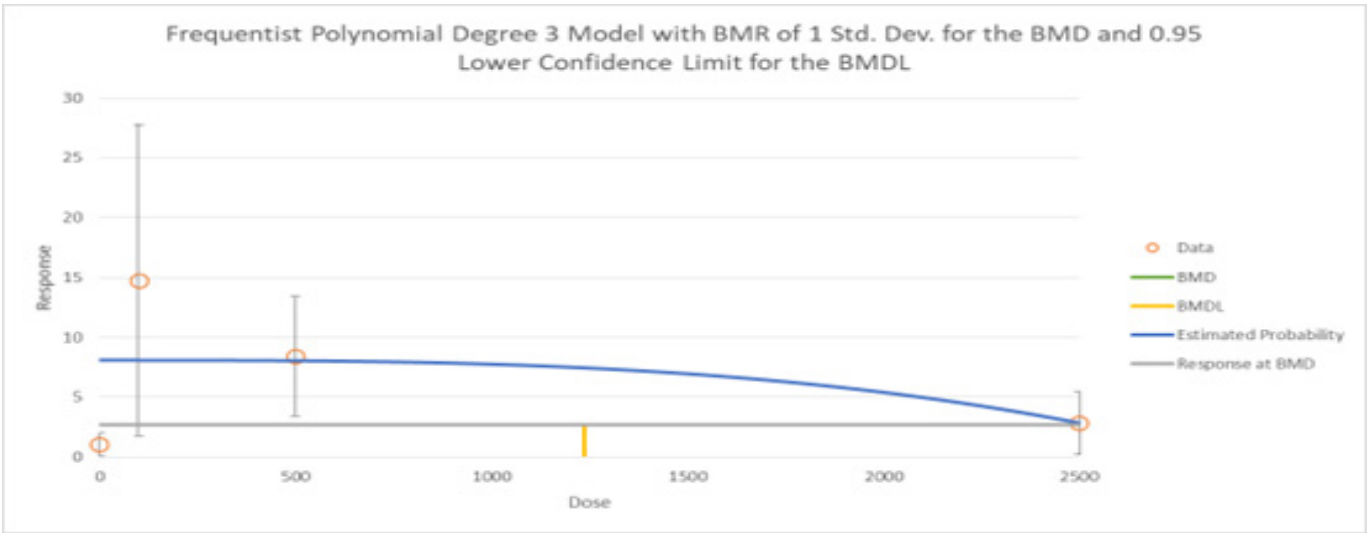

Figure5B: Expression of the Irs1 gene in AML12 cells in the lower chamber of the Transwell system after 48 hours of BPAF treatment

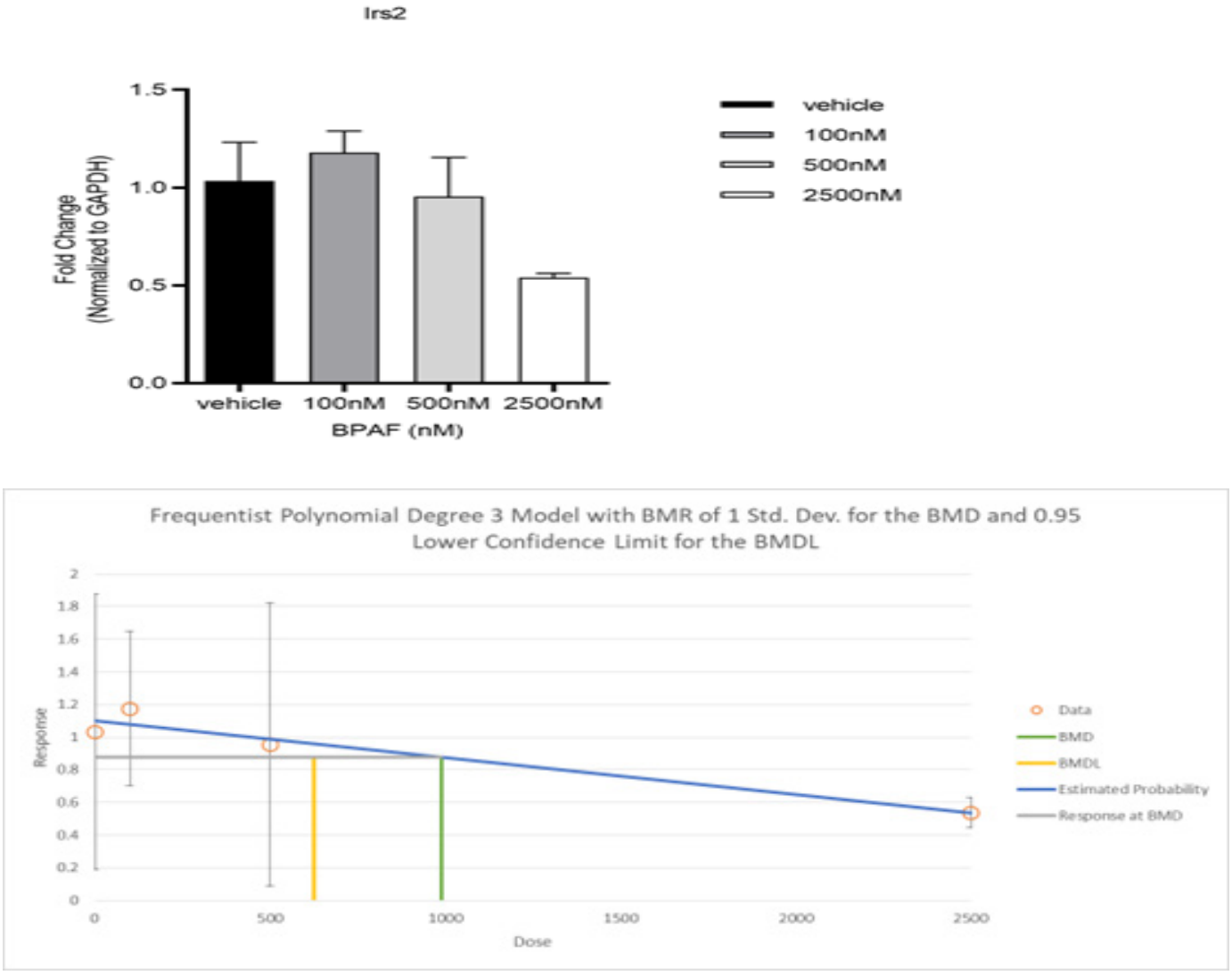

Figure5C: Expression of the Irs2 gene in AML12 cells in the lower chamber of the Transwell system after 48 hours of BPAF treatment

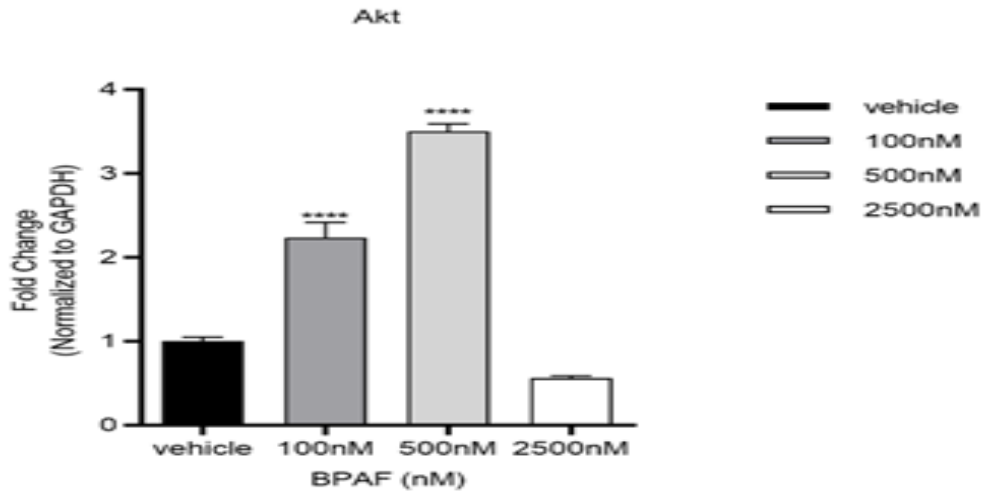

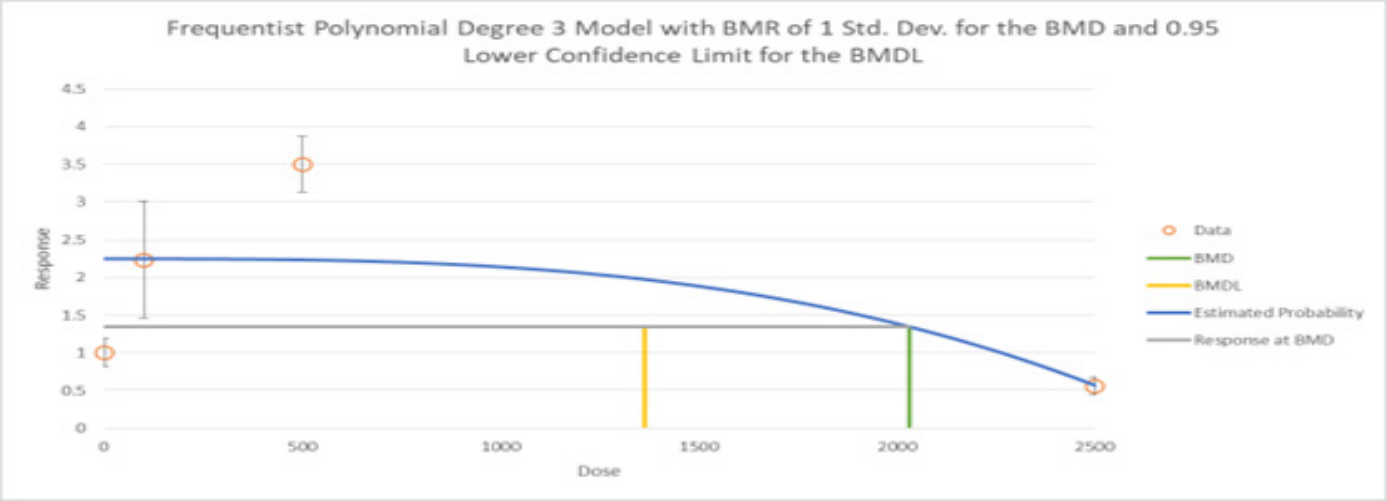

Figure5D: Expression of the Akt gene in AML12 cells in the lower chamber of the Transwell system after 48 hours of BPAF treatment

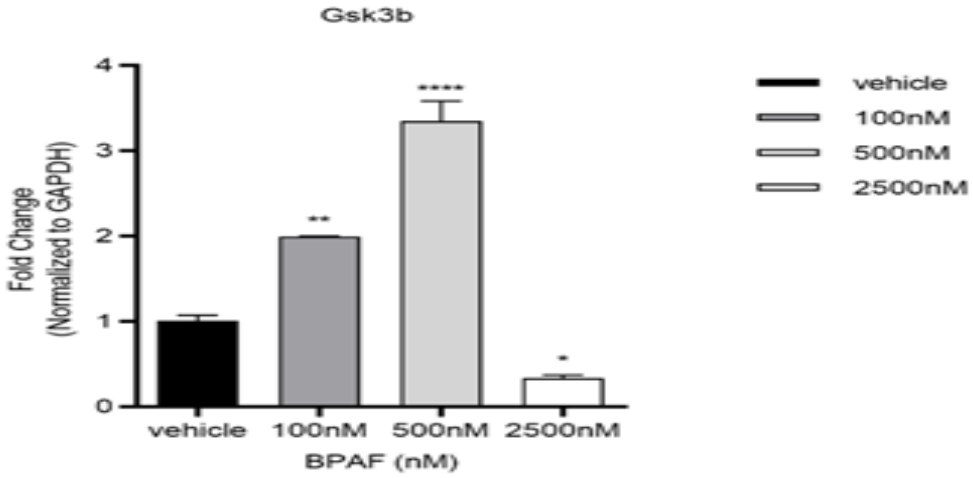

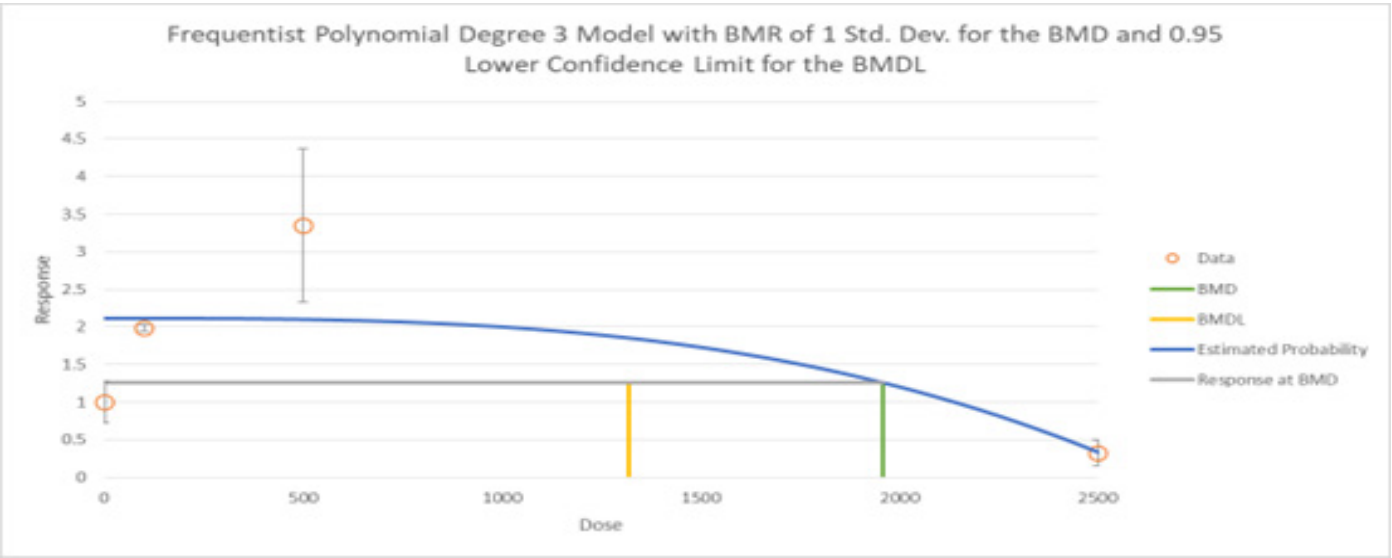

Figure5E: Expression of the Gsk3b gene in AML12 cells in the lower chamber of the Transwell system after 48 hours of BPAF treatment

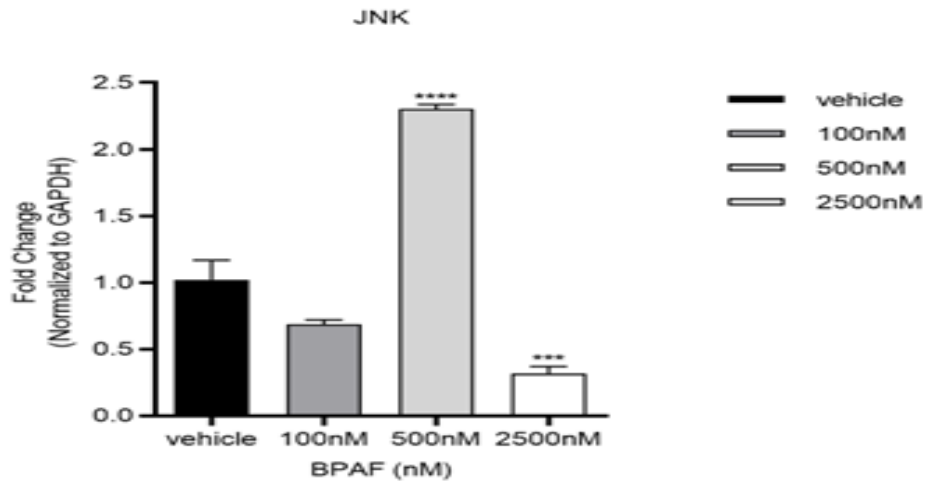

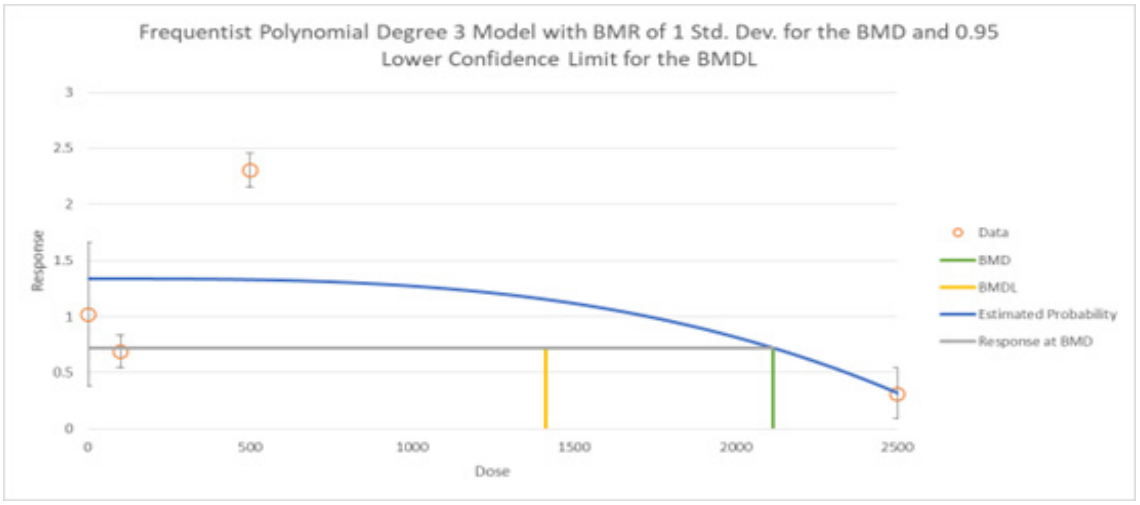

Figure5F: Expression of the JNK gene in AML12 cells in the lower chamber of the Transwell system after 48 hours of BPAF treatment

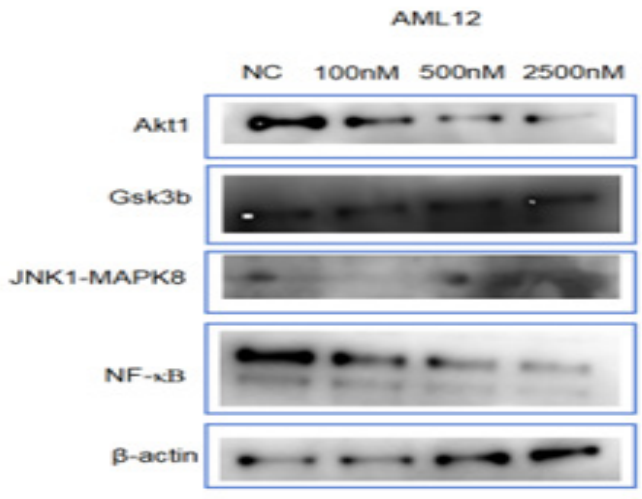

Figure5G: Protein expression in AML12 cells in the lower chamber of the Transwell system after 48 hours of BPAF treatment

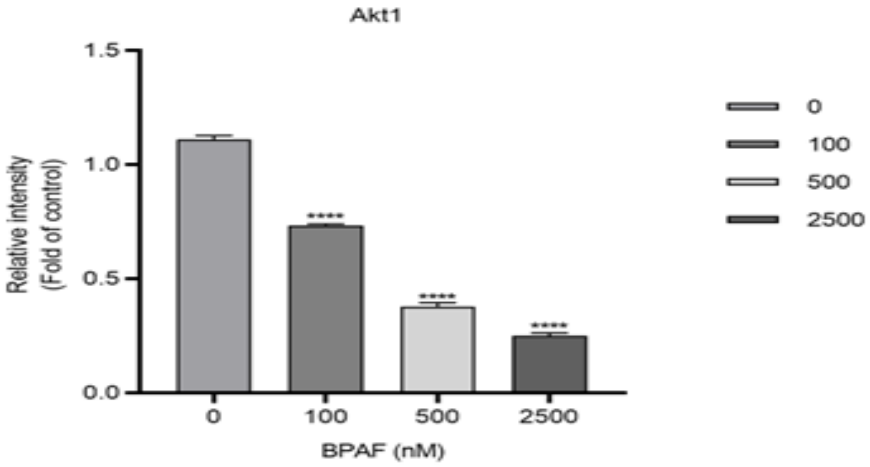

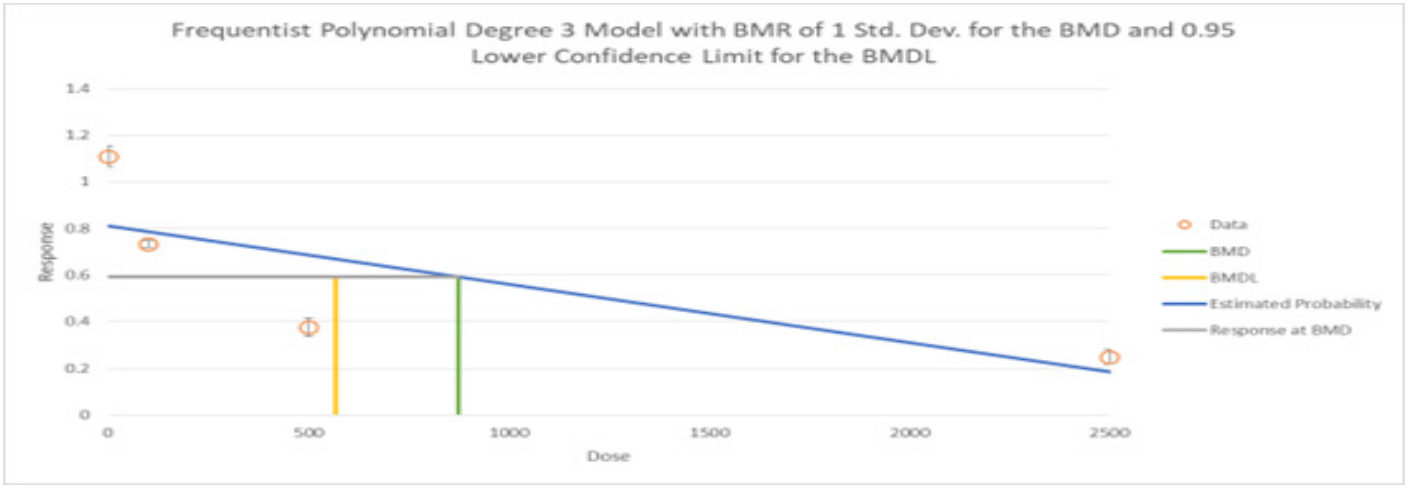

Figure5H: Grayscale analysis of Akt1

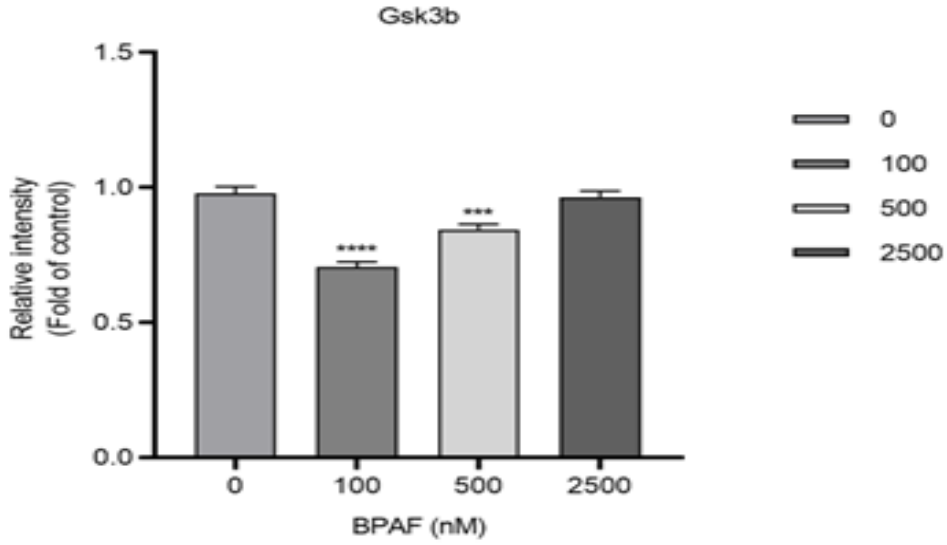

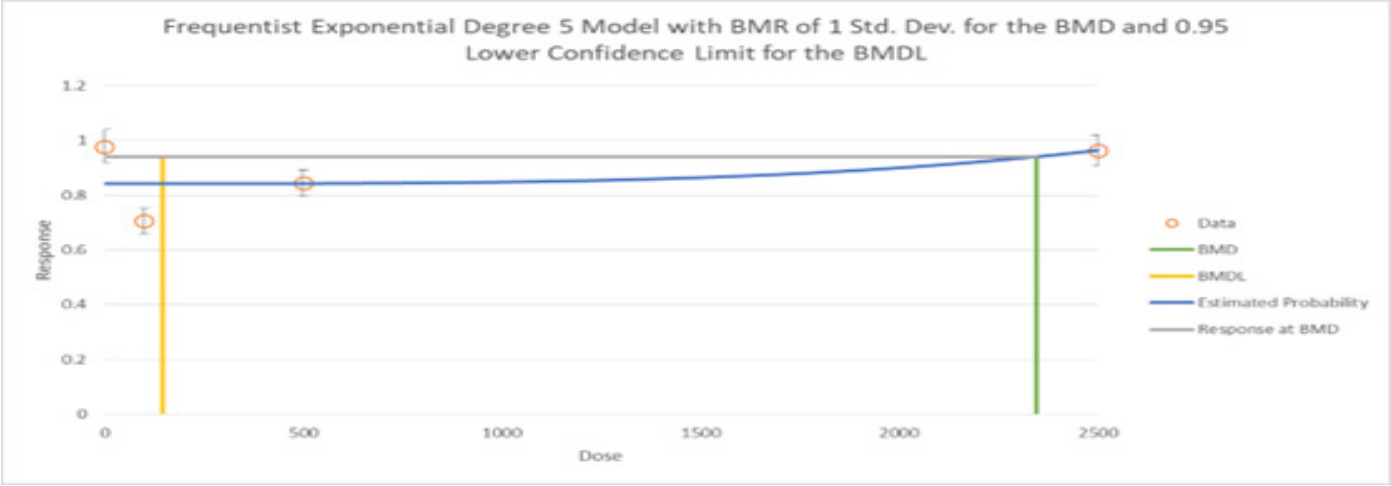

Figure5I: Grayscale analysis of Gsk3b

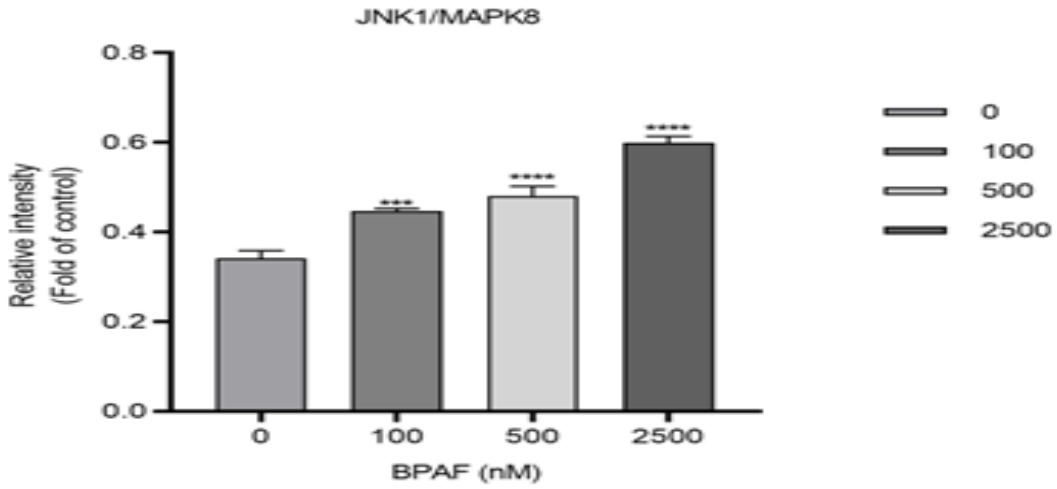

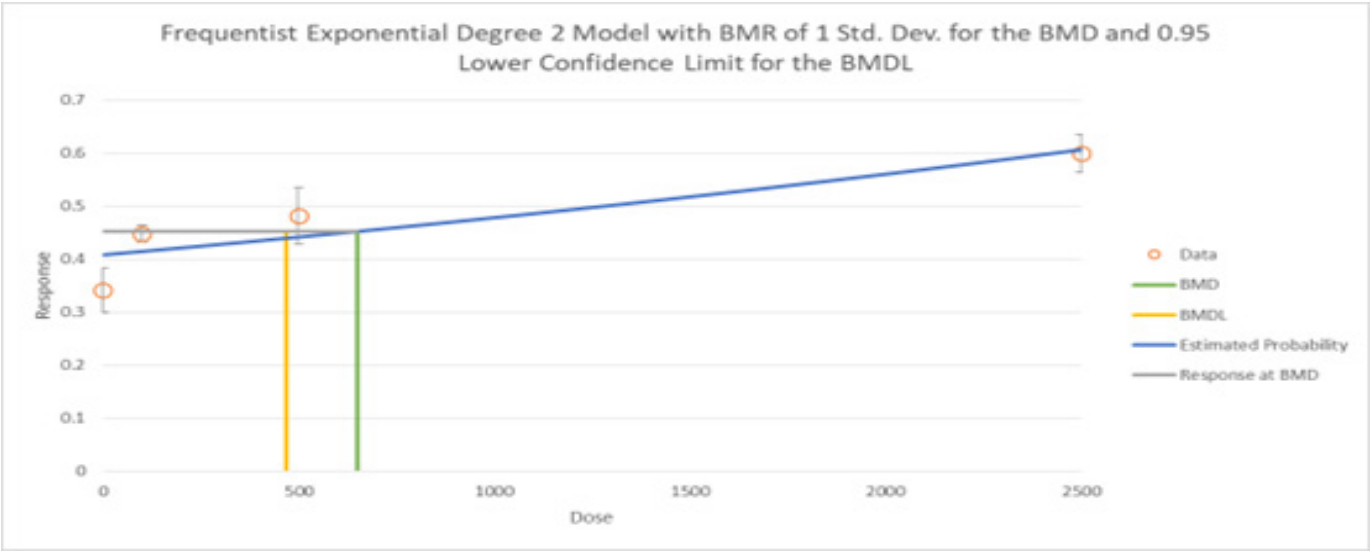

Figure5J: Grayscale analysis of JNK1/MAPK8

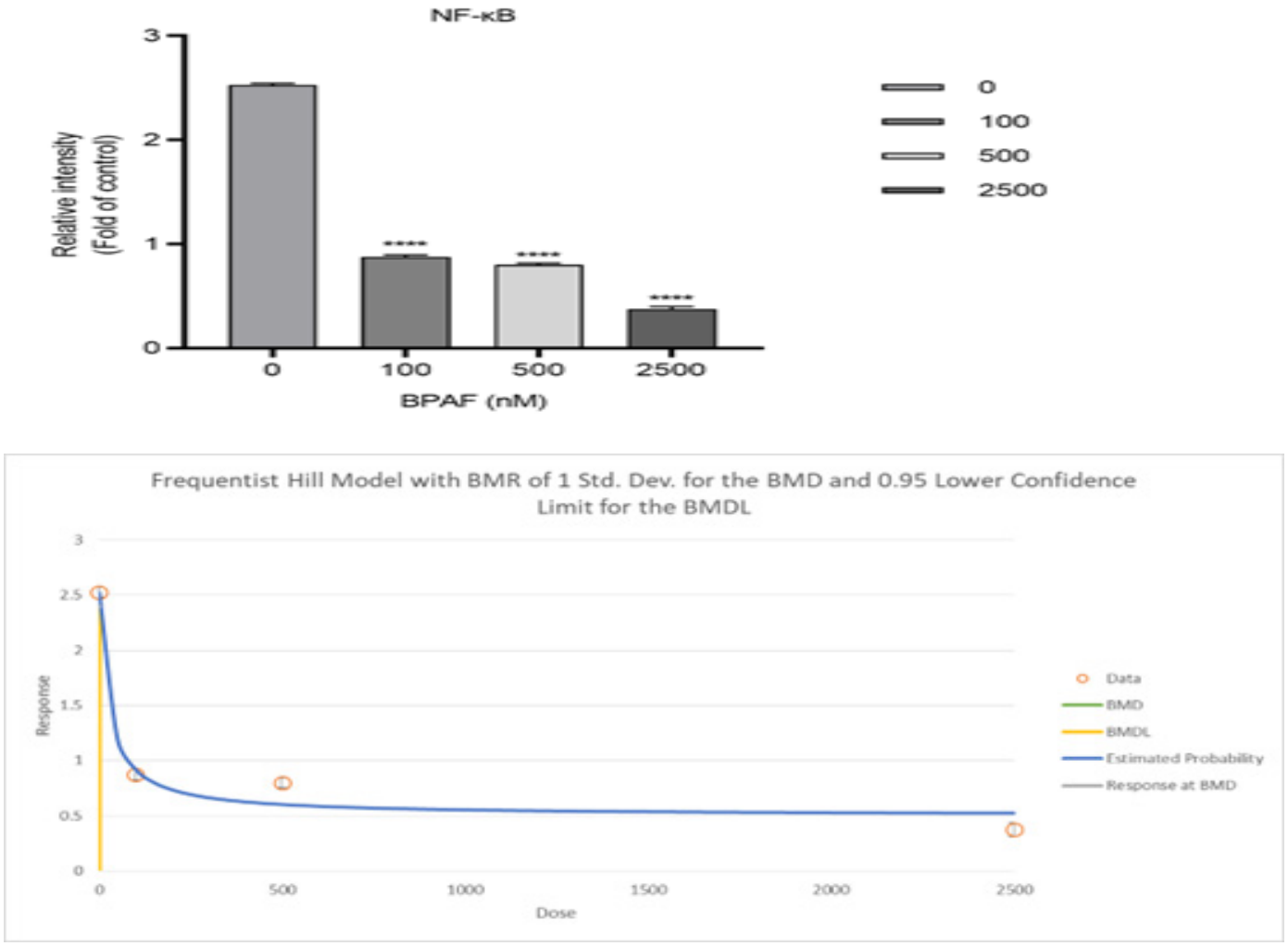

Figure5K: Grayscale analysis of NF-κB

The data represent the mean results of three independent experiments (mean ± SD).
(*: Compared with the negative control group, P < 0.05;
**: Compared with the negative control group, P < 0.01;
***: Compared with the negative control group, P < 0.001;
****: Compared with the negative control group, P < 0.0001)

Figure5: BPAF suppresses the expression of key molecules in the insulin signaling pathway.

Animal Experiment Verification: High doses of BPAF led to metabolic disorders, enhanced inflammatory responses, and insulin resistance in mice.

Body Weight Growth Curve

After 90 days of BPAF administration (0, 0.5, 4, and 32 mg/kg), there were no significant differences in body weight among the dose groups in C57BL/6J mice (F values were -1.179, 0.1410, and -1.462; P values were 0.4020, 0.9970, and 0.2388, respectively) (Figure 6A).

Liver Weight and Organ Index

After 90 days of BPAF administration (0, 0.5, 4, and 32 mg/kg), there were no significant differences in liver weight among the dose groups in C57BL/6J mice (F values were -0.07450, -0.007833, and 0.06917; P values were 0.8986, 0.9998, and 0.9161, respectively). There were also no significant differences in the liver-to-body weight ratio among the dose groups in C57BL/6J mice (F values were -0.0001667, -0.0003333, and 0.006333; P values were >0.9999, 0.9998, and 0.4542, respectively) (Figure 6B).

Biochemical Analysis of Blood

After 90 days of BPAF administration (0, 0.5, 4, and 32 mg/kg), serum levels of AST, ALT, ALP, TG, and CHOL showed no significant differences compared to the control group ($p > 0.05$). Biochemical analysis of blood indicated that, compared to the control group, fasting blood glucose and hepatic triglyceride levels in the BPAF-exposed group showed no significant differences ($p > 0.05$), while indicators of insulin sensitivity (NEFA and D3H) exhibited a downward trend (Figure 6). The levels of HS-CRP were significantly decreased among the dose groups in C57BL/6J mice (F values were 0.4507, 0.5081, and 0.5559; P values were <0.0001, <0.0001, and <0.0001, respectively). The levels of TNF-α were significantly increased among the dose groups in C57BL/6J mice (F values were -26.24, -29.92, and -41.76; P values were <0.0001, <0.0001, and <0.0001, respectively). The levels of IL-1β were significantly increased among the dose groups in C57BL/6J mice (F values were -586.0, -725.3, and -1638; P values were 0.0067, 0.0018, and <0.0001, respectively). The levels of IL-6 were significantly increased among the dose groups in C57BL/6J mice (F values were -47.06, -339.4, and -578.0; P values were 0.0891, <0.0001, and <0.0001, respectively) (Figure 6).

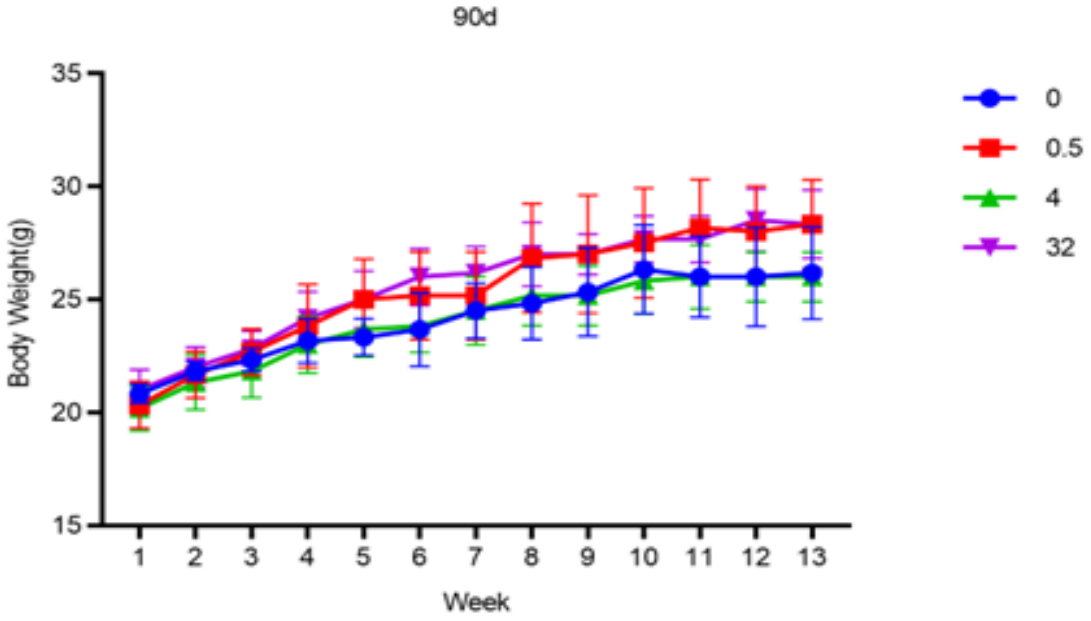

Figure6A: Body weight growth curve

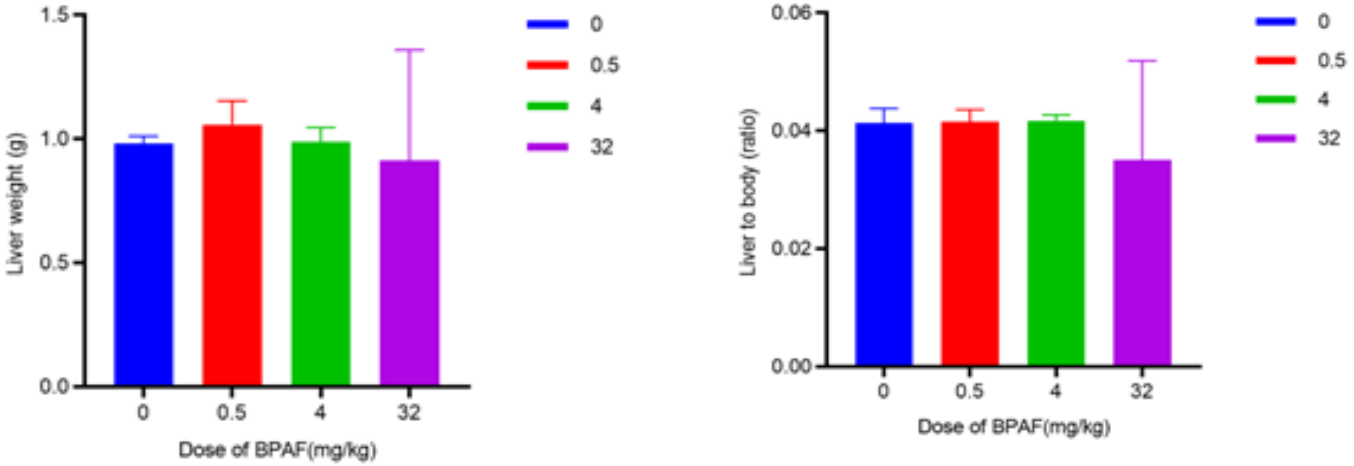

Figure6B: Liver weight and organ index

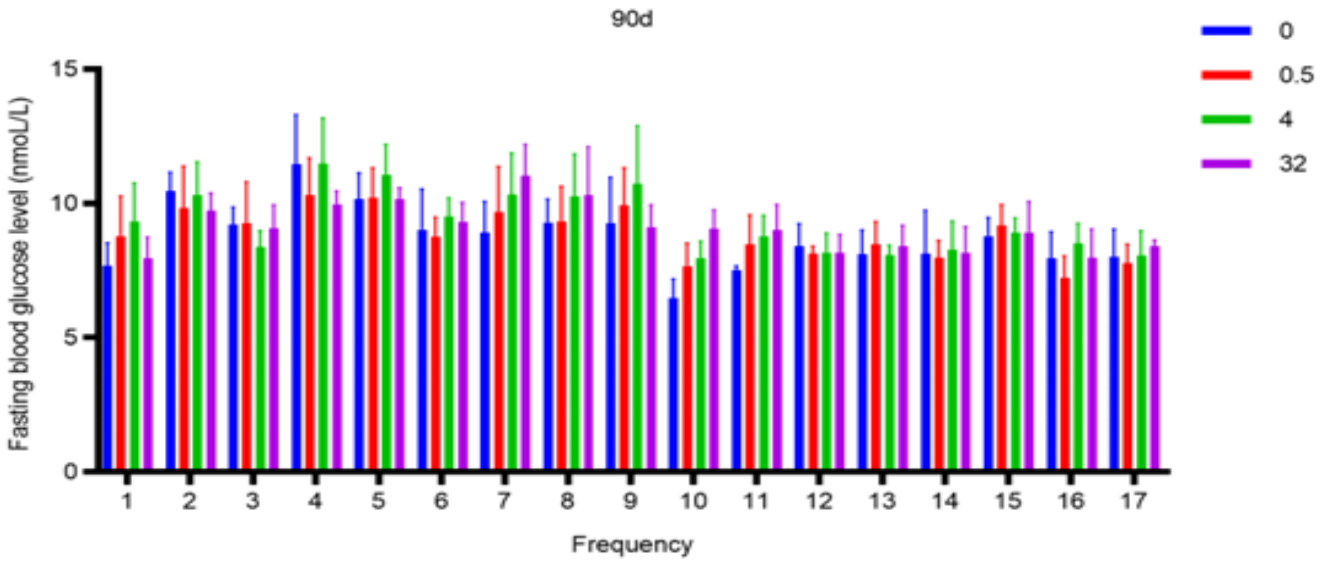

Figure6C: Biochemical analysis of blood

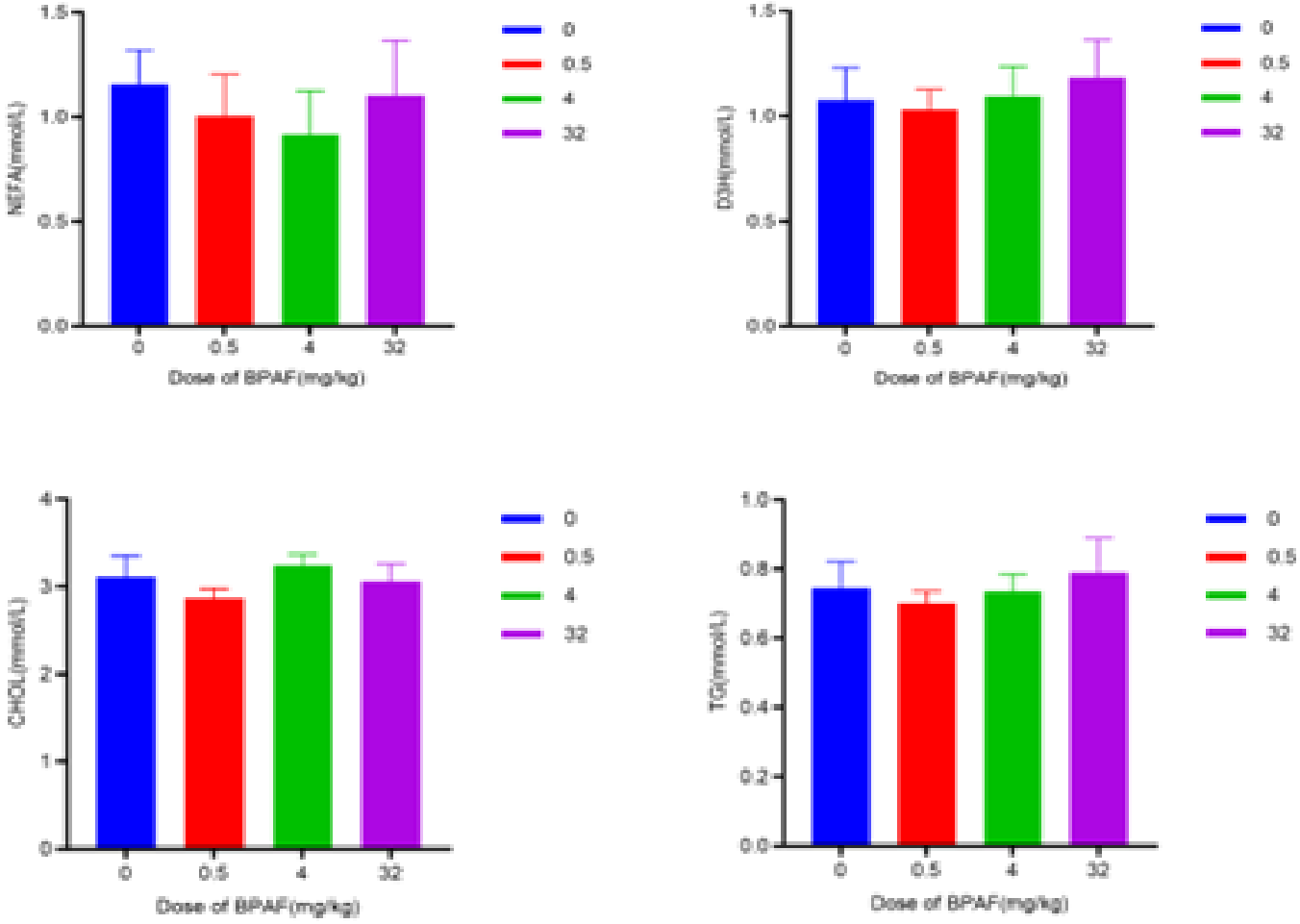

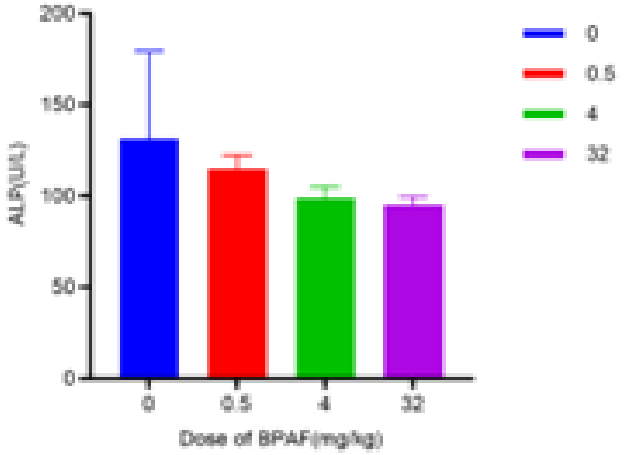
ALP(U/L)
200
150
100
50
0
0
0.5
4
32
Dose of BPAF(mg/kg)
0
0.5
4
32

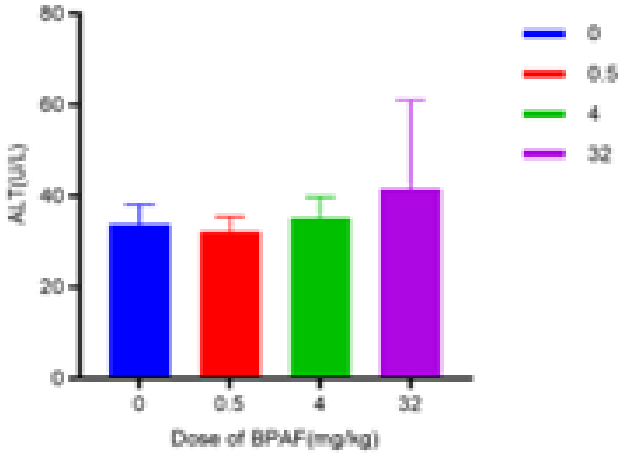
ALT(U/L)
80
60
40
20
0
0
0.5
4
32
Dose of BPAF(mg/kg)
0
0.5
4
32

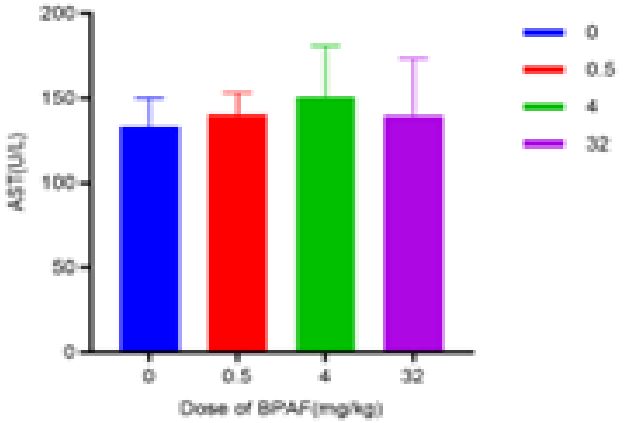
AST(U/L)
200
150
100
50
0
0
0.5
4
32
Dose of BPAF(mg/kg)
0
0.5
4
32

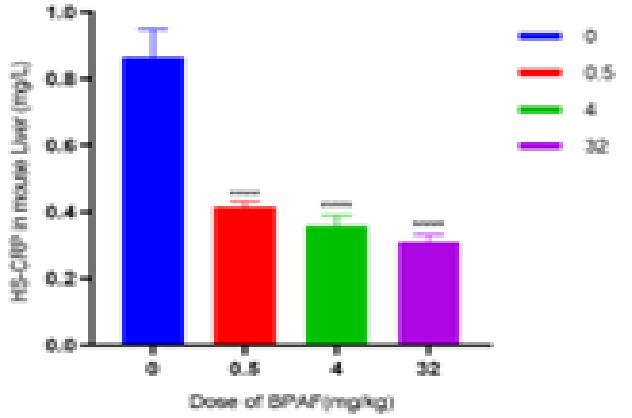
HS-CRP in mouse Liver (mg/L)
1.0
0.8
0.6
0.4
0.2
0.0
****
****
****
0
0.5
4
32
Dose of BPAF(mg/kg)
0
0.5
4
32

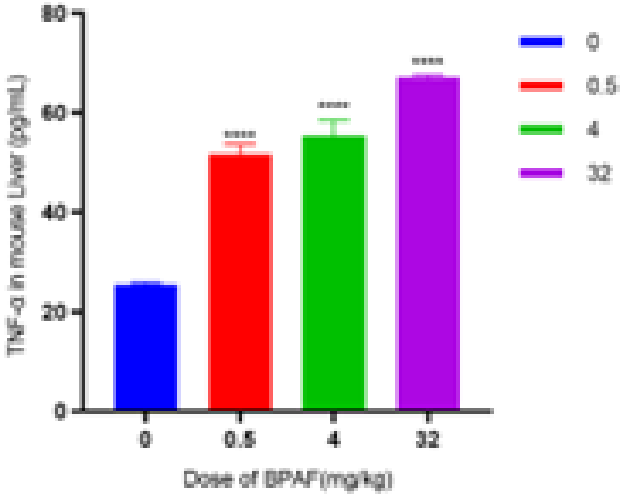
TNF-α in mouse Liver (pg/mL)
80
60
40
20
0
****
****
****
0
0.5
4
32
Dose of BPAF(mg/kg)
0
0.5
4
32

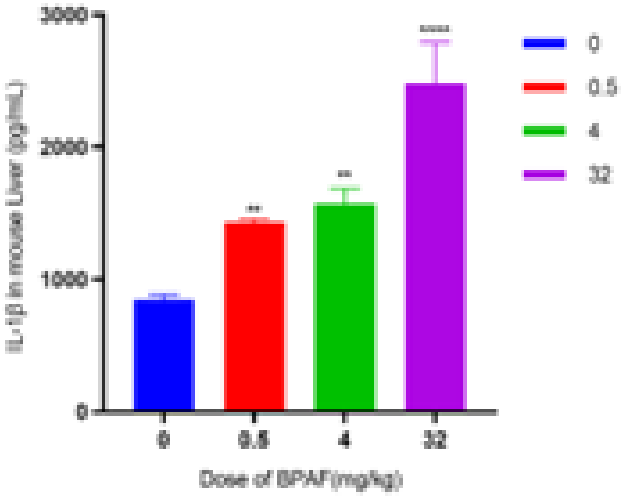
IL-1β in mouse Liver (pg/mL)
3000
2000
1000
0
**
**
****
0
0.5
4
32
Dose of BPAF(mg/kg)
0
0.5
4
32

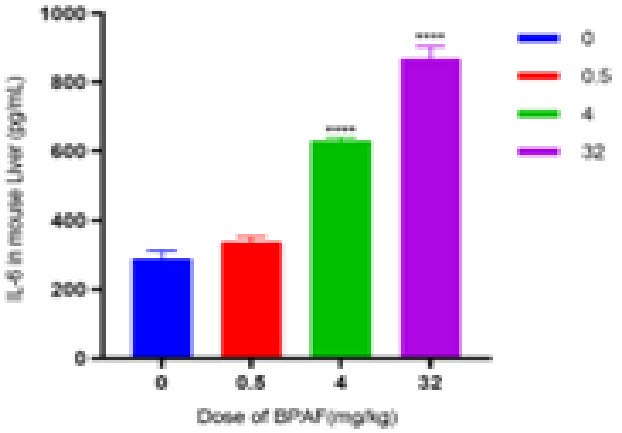

Figure6D: Blood glucose measurement

The data represent the mean results from 6 mice per group (mean ± SD). (*: Compared with the negative control group, P < 0.05; **: Compared with the negative control group, P < 0.01; ***: Compared with the negative control group, P < 0.001; ****: Compared with the negative control group, P < 0.0001)

Real-Time Quantitative PCR

After 90 days of gavage with BPAF (32 mg/kg) in C57BL/6J mice, the gene expression of JNK and Insr in liver tissues was significantly upregulated (BMD = 14.45 mg/kg and 202.70 mg/kg, respectively; Figure 7).

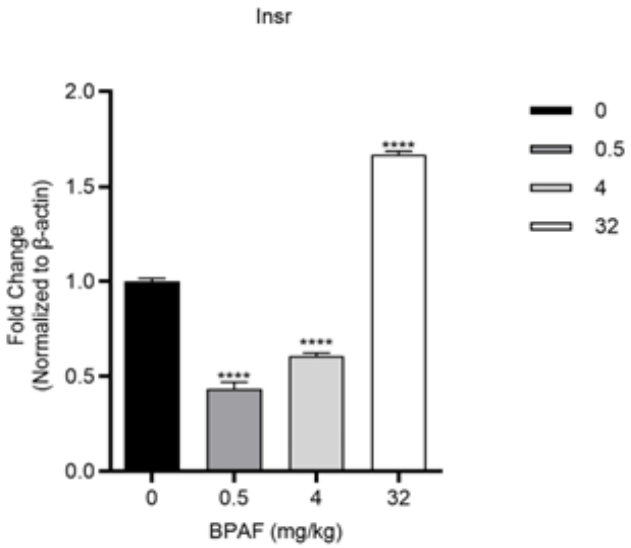

Figure6: A 90-day oral toxicity study of BPAF in C57BL/6J mice.

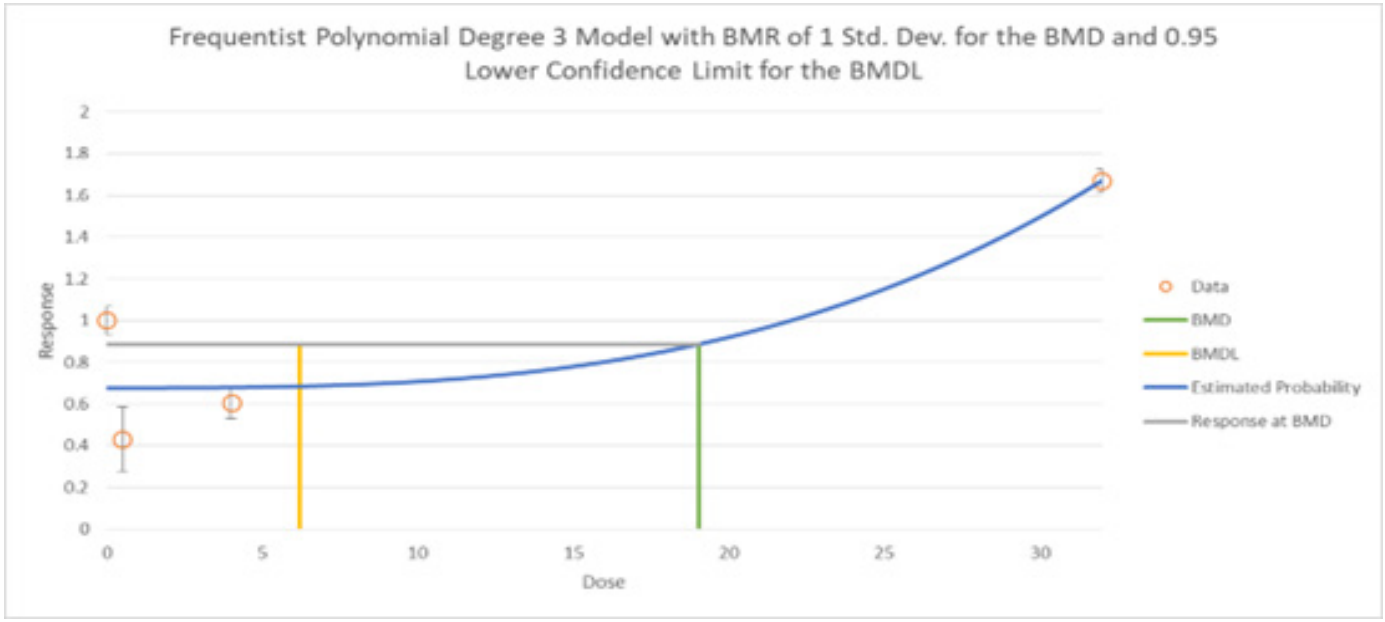

Figure7A: Gene expression of Insr

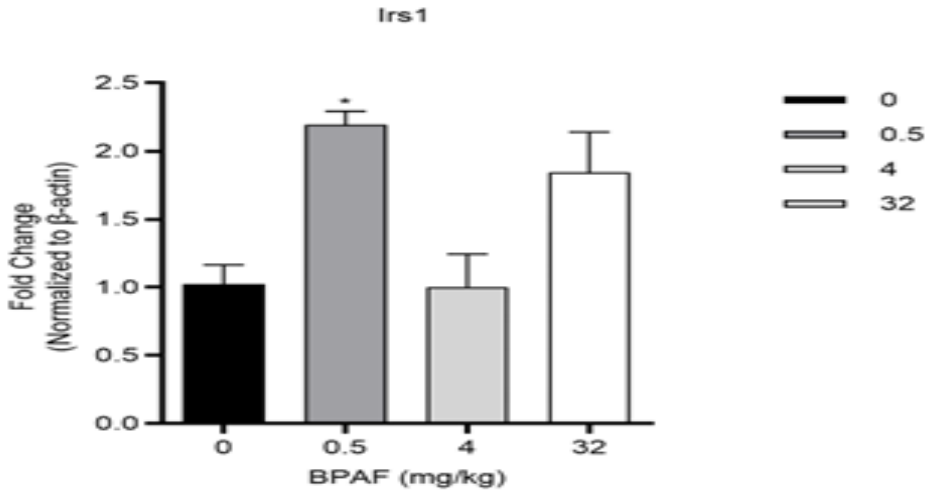

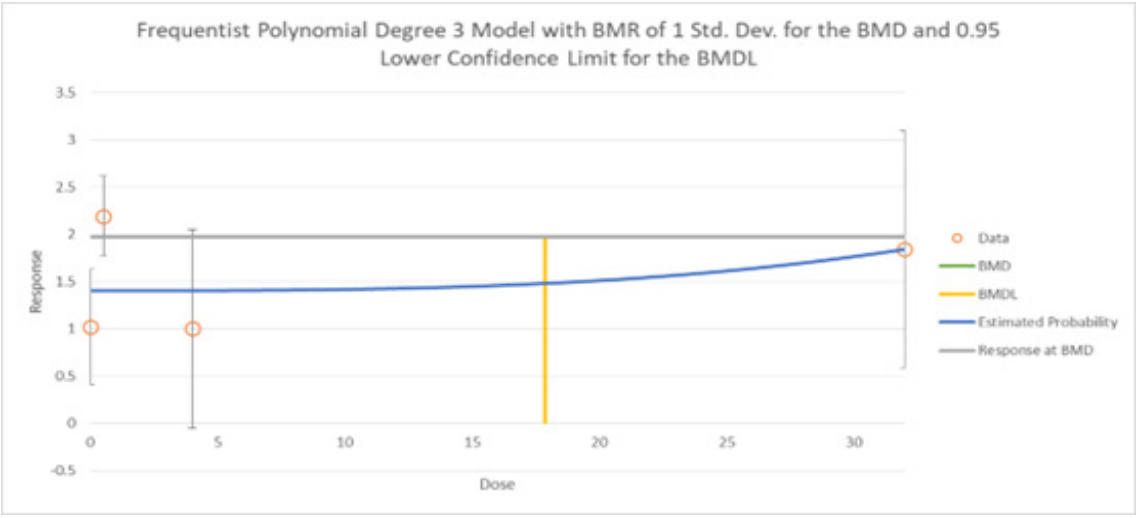

Figure7B: Gene expression of Irs1

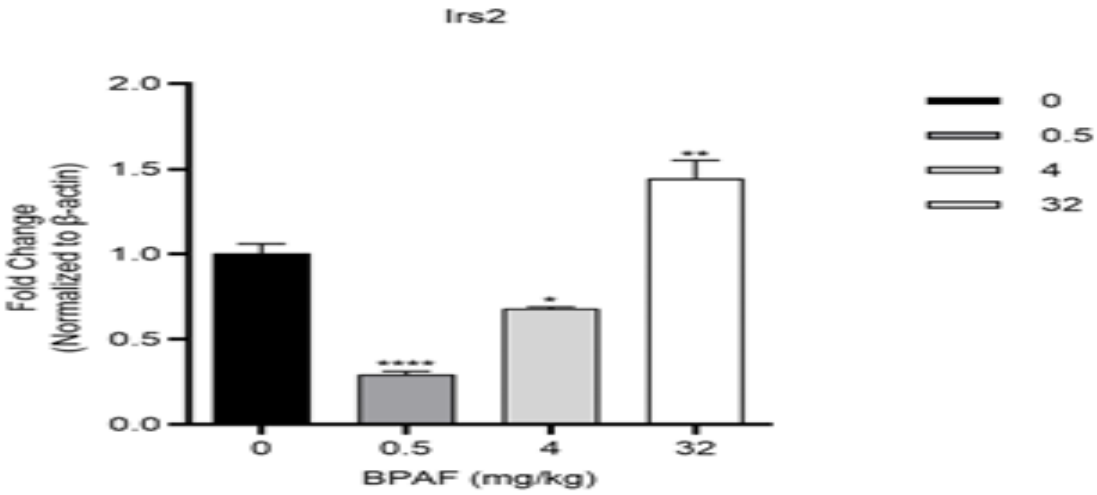

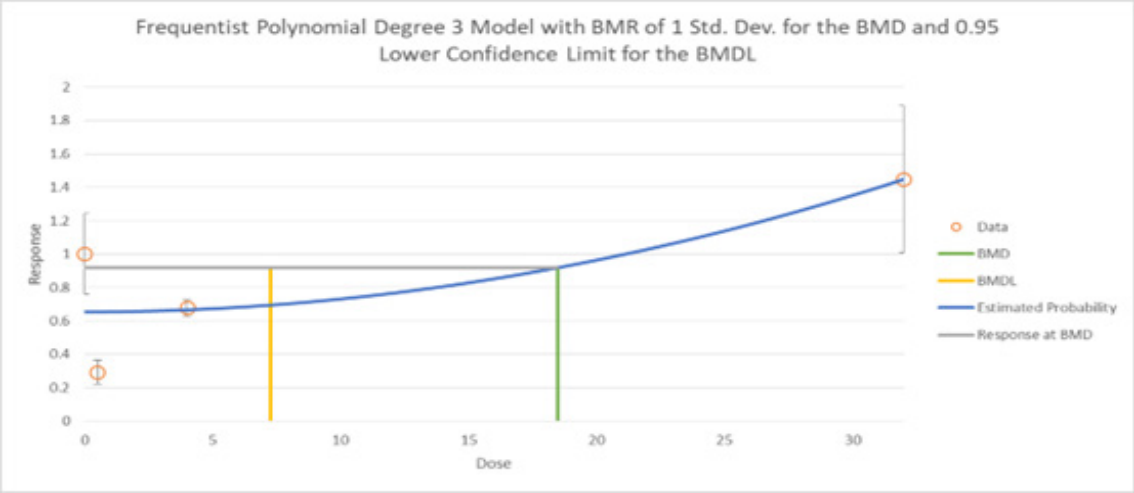

Figure7C: Gene expression of Irs2

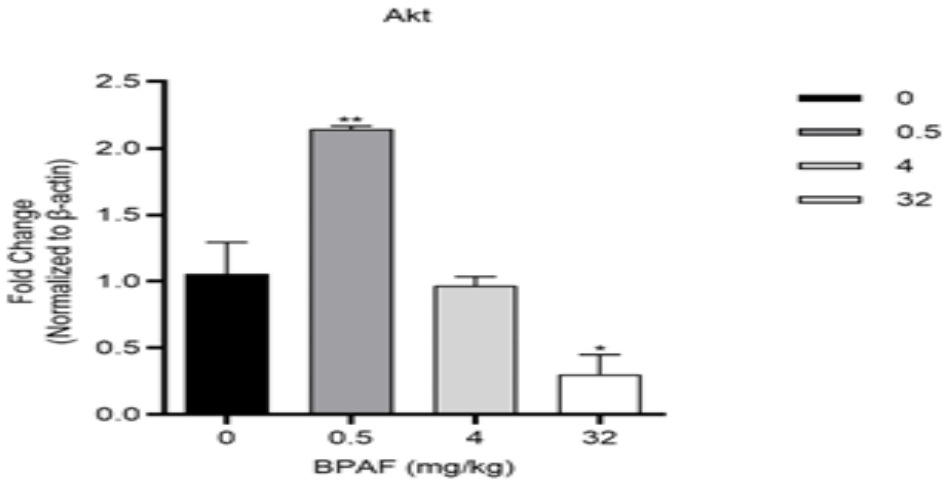

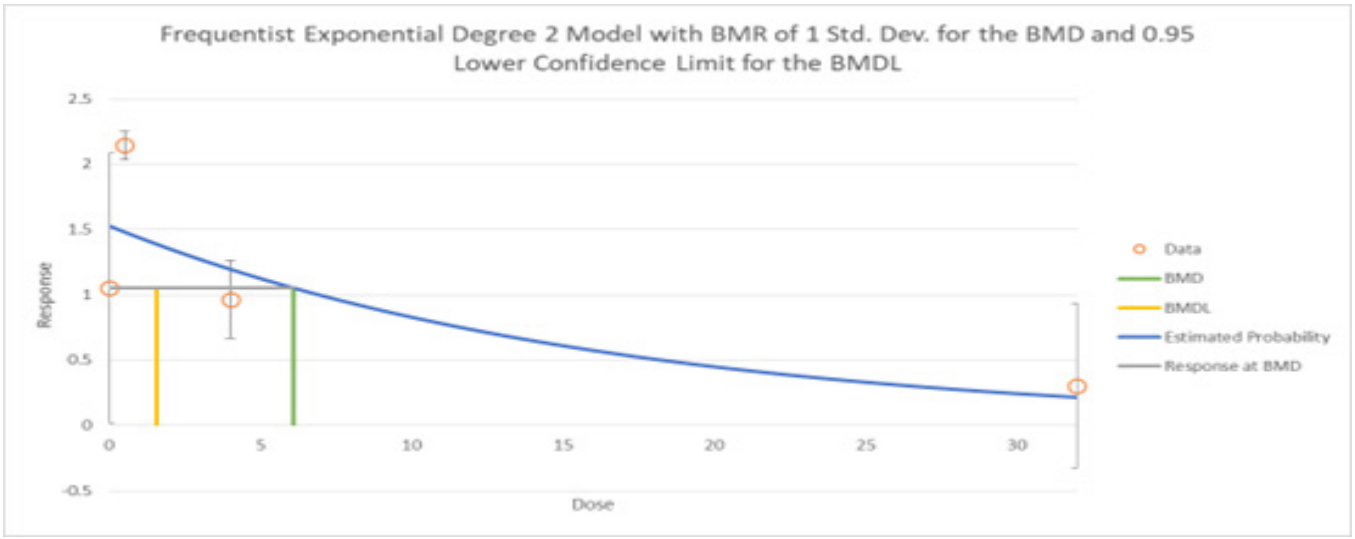

Figure7D: Gene expression of Akt

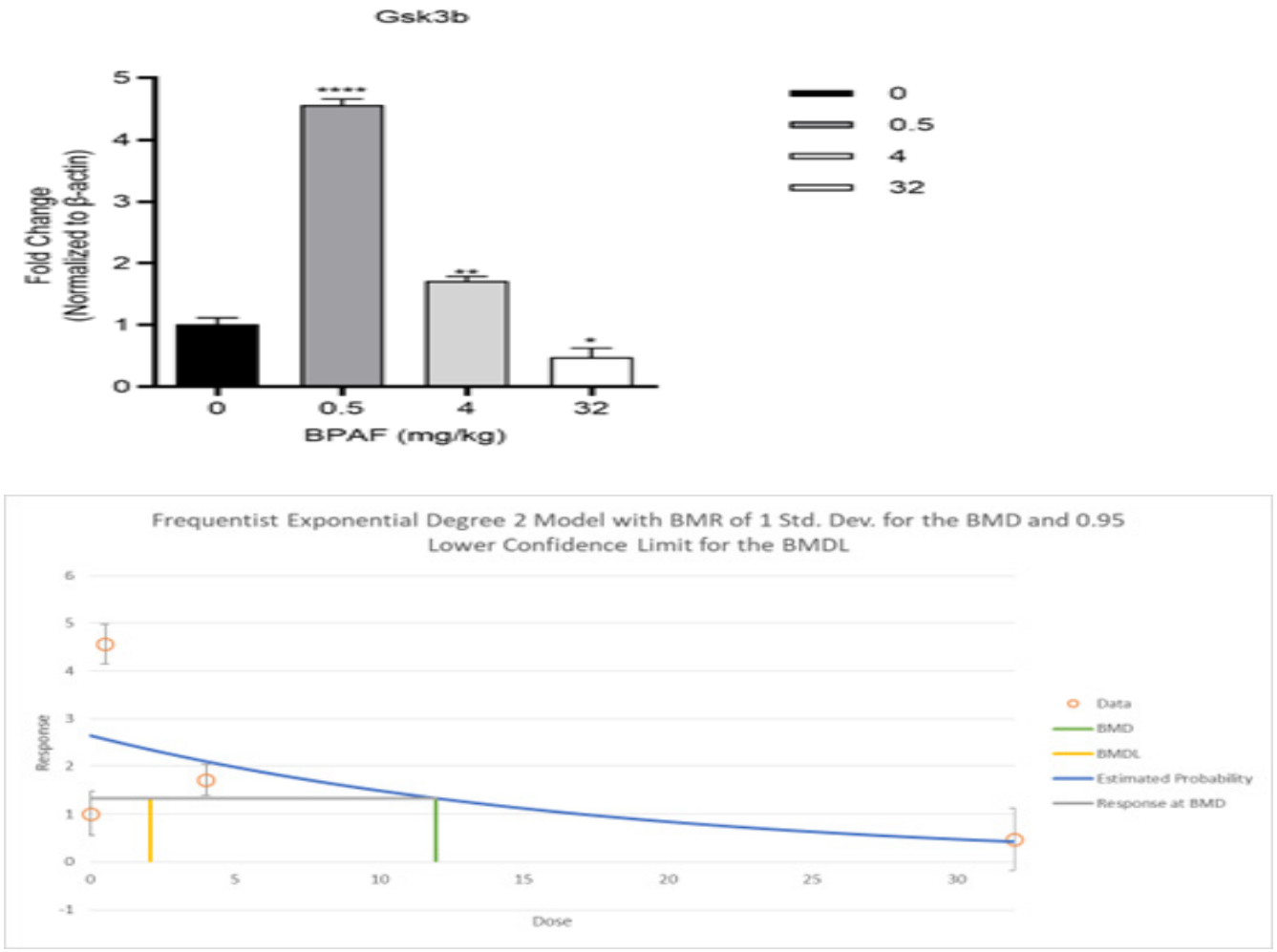

Figure7E: Gene expression of Gsk3b

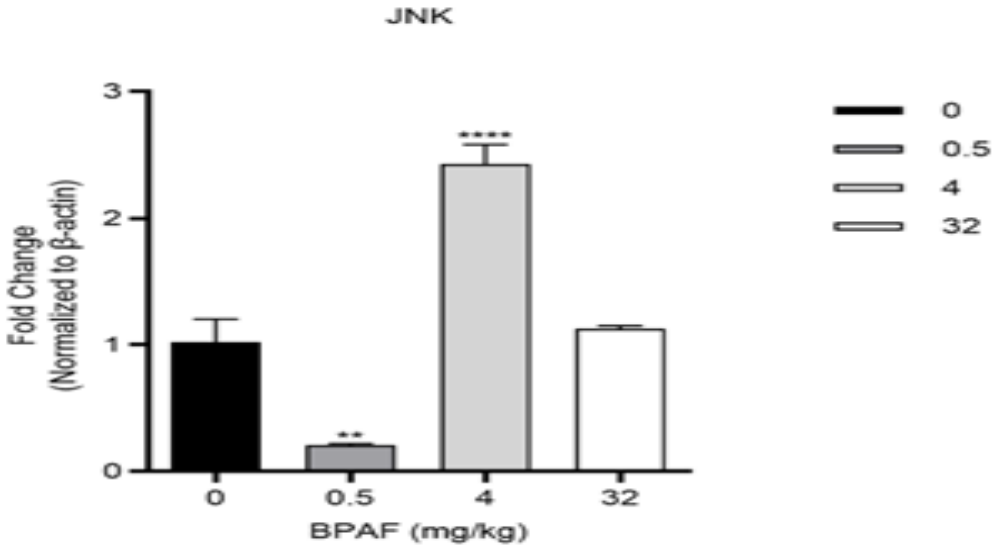

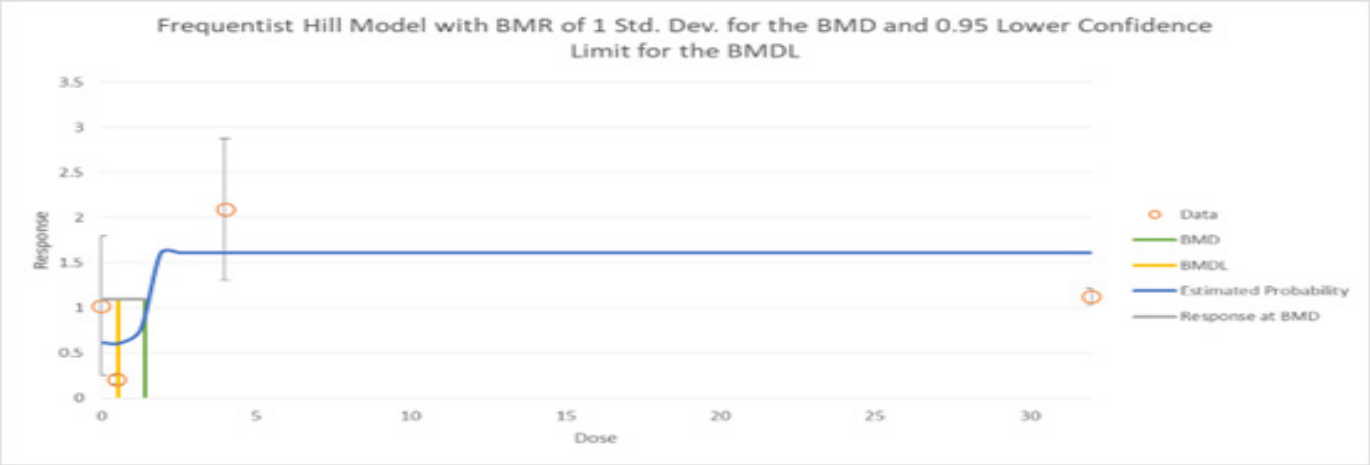

Figure7F: Gene expression of JNK

The data represent the mean results from 6 mice per group (mean ± SD).
(*: Compared with the negative control group, P < 0.05;
**: Compared with the negative control group, P < 0.01;
***: Compared with the negative control group, P < 0.001;
****: Compared with the negative control group, P < 0.0001)

Figure7: BPAF-induced Real-time qPCR detection of liver tissue.

Hematoxylin and Eosin (H&E) Staining and Oil Red O Staining

After 90 days of BPAF administration (0, 0.5, 4, 32 mg/kg), hematoxylin and eosin (H&E) staining of liver tissues from C57BL/6J mice showed no significant pathological changes (Figure 8). The specific observations were as follows: the liver lobule structure was clear, and hepatocytes were arranged in an orderly manner, with no obvious necrotic areas or cell detachment observed. The nuclei of hepatocytes were uniform in size, with intact nuclear membranes, and no significant nuclear pyknosis, fragmentation, or dissolution was noted. No significant inflammatory cell infiltration (such as lymphocytes or neutrophils) was observed in the liver tissue. The cytoplasm of hepatocytes showed no obvious lipid droplet accumulation (indicating no fatty degeneration), and there was no evidence of fibrosis in the interstitium.

Oil Red O staining results showed that with increasing doses of BPAF, the number and size of red lipid droplets in the liver tissue gradually increased. Specifically, in the 4 mg/kg and 32 mg/kg dose groups, the number of red lipid droplets began to increase significantly, and their size became larger, indicating the presence of lipid accumulation in the liver tissue at higher doses (Figure 8).

Immunofluorescence Staining of Frozen Sections

After 90 days of BPAF administration, compared with the control group, the highest dose group (32 mg/kg) showed nuclear translocation of NF-κB with a significant increase in fluorescence intensity ($t = 74.54$, $df = 8$, $P < 0.0001$) (Figure 8).

Fluorescence Microplate Reader Analysis of M1 and M2 Macrophage Ratios

After 90 days of BPAF administration (0, 0.5, 4, and 32 mg/kg), compared with the control group, the fluorescence intensity ratio of M1 and M2 macrophages in the highest dose group (32 mg/kg) was significantly increased (F values were -0.1599, -0.1565, and -0.8968; P values were 0.5155, 0.4530, and 0.0011, respectively) (Figure 8).

Transmission Electron Microscopy

In the liver tissues of mice treated with BPAF (32 mg/kg, 90 days), significant abnormalities in mitochondrial morphology were observed under transmission electron microscopy (TEM). The mitochondria exhibited increased volume and expanded matrix, potentially accompanied by vacuolization of the inner cavity. The mitochondrial cristae were fragmented, blurred, or completely disappeared, leading to a reduction in the surface area of the inner membrane and impairing energy metabolism function. Rupture of the outer or inner mitochondrial membranes was observed, possibly accompanied by increased membrane permeability, triggering apoptotic signaling. The electron density of the mitochondrial matrix was reduced, indicating impaired metabolic activity. Additionally, swelling of the endoplasmic reticulum, lipid droplet accumulation, or the formation of autophagosomes might be observed, reflecting cellular stress responses (Figure 8).

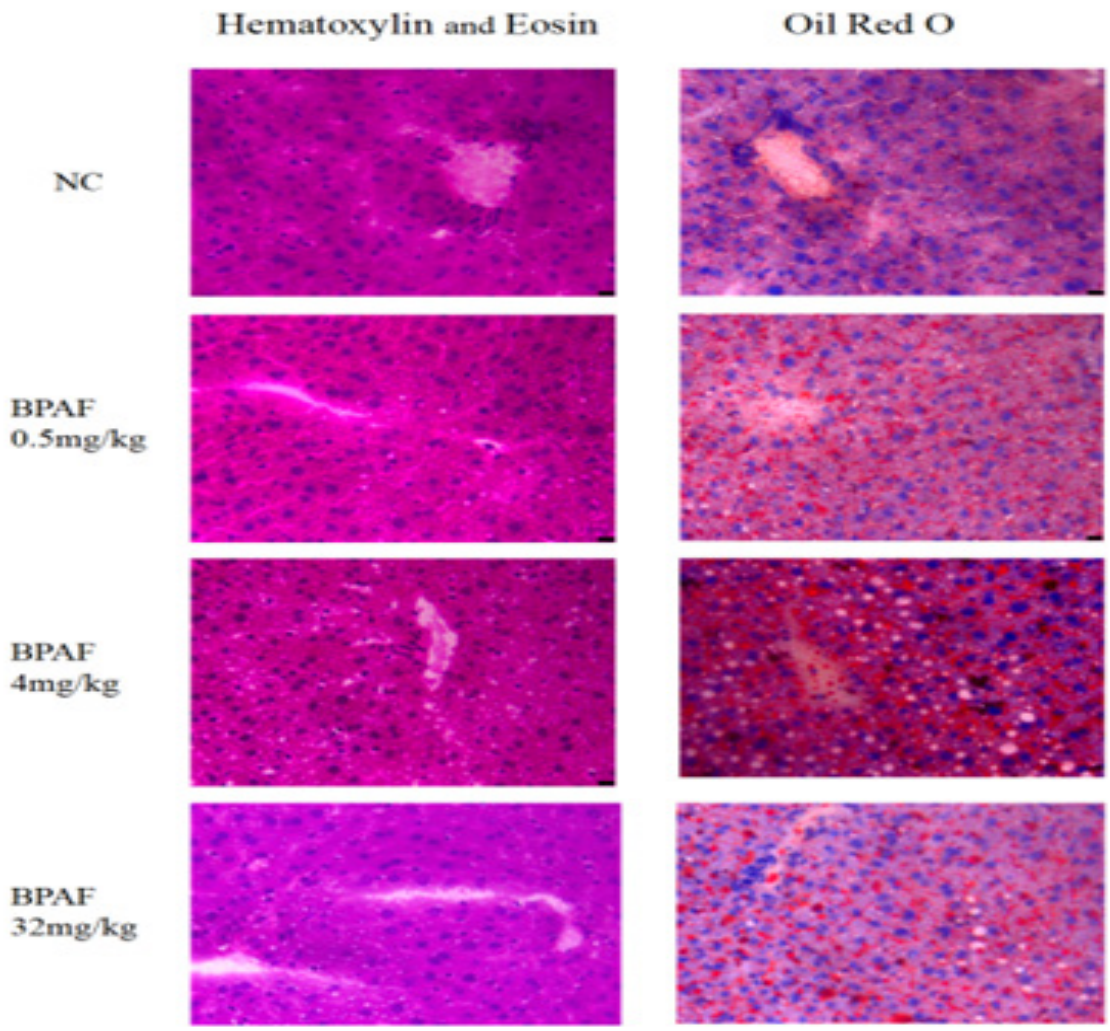

Figure8A: Hematoxylin and eosin (H&E) staining

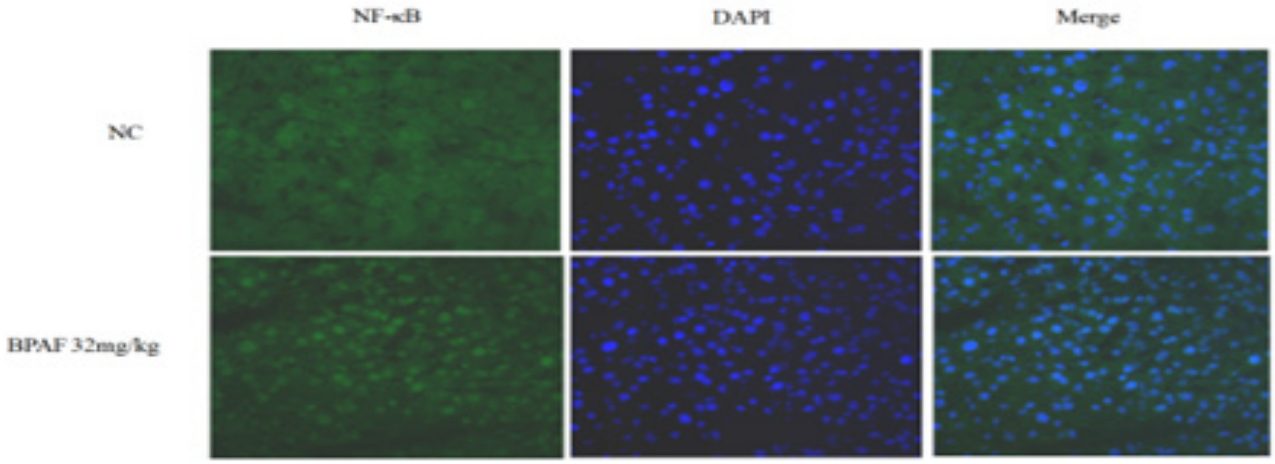

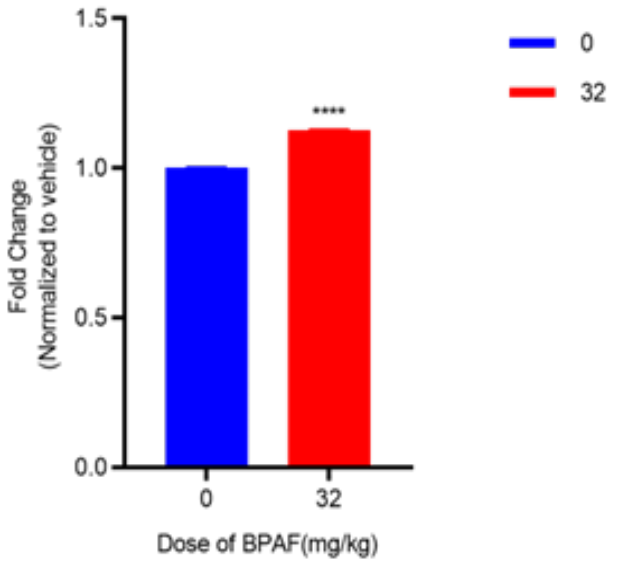

Figure8B: Immunofluorescence staining of NF-κB in frozen sections

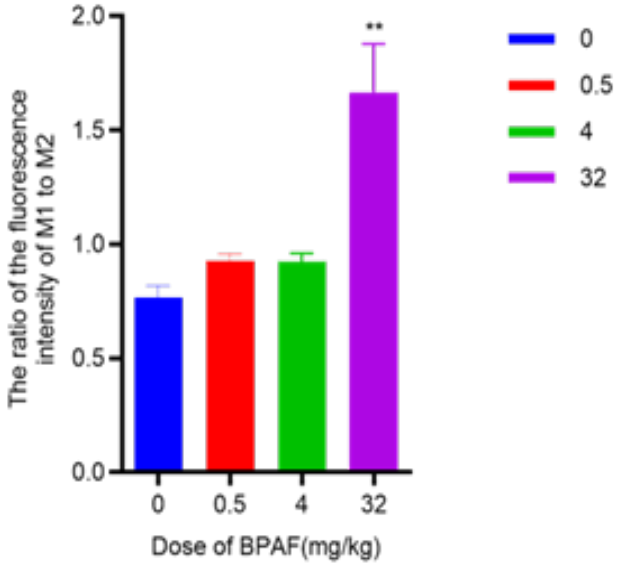

Figure8C: Fluorescence microplate reader analysis of the fluorescence intensity ratio changes of M1 and M2 macrophages

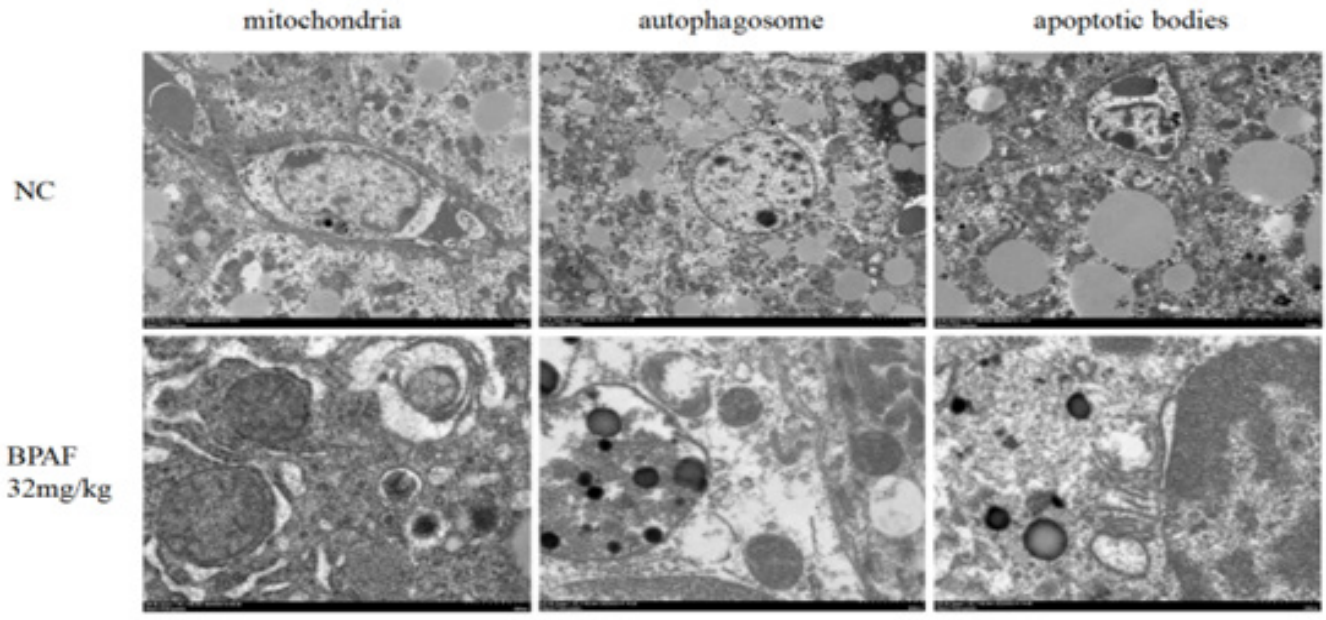

Figure8D: Transmission electron microscopy

The data represent the mean results from 6 mice per group (mean ± SD).
(*: Compared with the negative control group, P < 0.05;
**: Compared with the negative control group, P < 0.01;
***: Compared with the negative control group, P < 0.001;
****: Compared with the negative control group, P < 0.0001)

Figure8: Pathology analysis of a 90-day oral toxicity study of BPAF in C57BL/6J mice.

Discussion

Bisphenol AF (BPAF), a persistent endocrine disruptor, disrupts hepatic insulin sensitivity through multifaceted mechanisms involving mitochondrial-associated endoplasmic reticulum membranes (MAMs) dysfunction, inter-organ metabolic crosstalk, and inflammatory amplification. As illustrated in Figure 9, these pathways synergistically impair insulin signaling, exacerbate oxidative stress, and perpetuate a pro-inflammatory milieu, ultimately driving hepatic insulin resistance (IR).

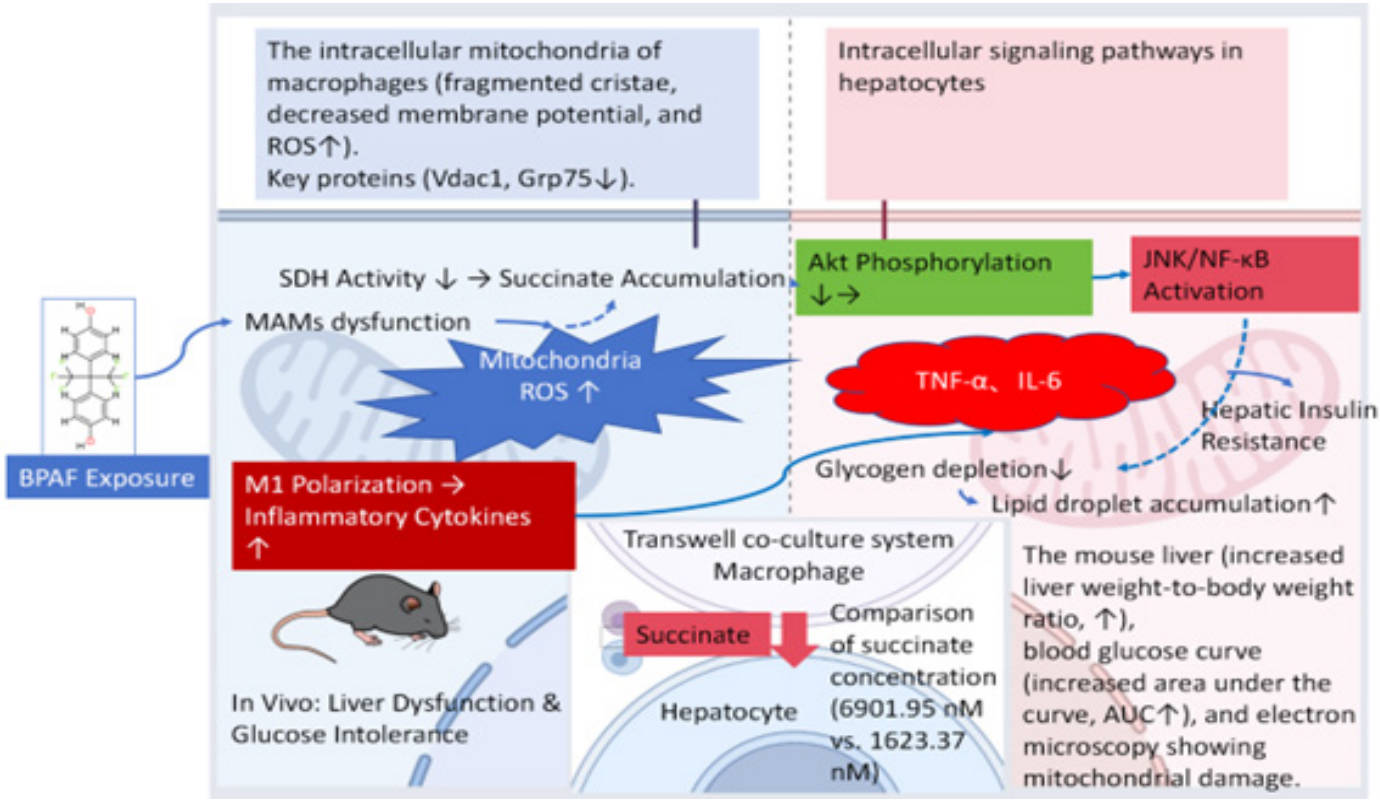

Figure9: Molecular Mechanisms of BPAF-Induced Hepatic Insulin Resistance

MAMs Dysfunction and ER-Mitochondrial Miscommunication

MAMs serve as critical hubs for lipid transfer, calcium signaling, and metabolic coordination between the endoplasmic reticulum (ER) and mitochondria. BPAF disrupts MAMs integrity, leading to: ER Stress and JNK Activation: BPAF induces ER stress by overloading the organelle with misfolded proteins or lipid intermediates (e.g., ceramides), triggering the unfolded protein response (UPR). This activates c-Jun N-terminal kinase (JNK), which phosphorylates insulin receptor substrate-1 (IRS-1) on inhibitory serine residues (Ser307), blocking insulin-mediated tyrosine phosphorylation and downstream Akt activation [16]. Mitochondrial Dysfunction: Impaired MAMs reduce mitochondrial oxidative capacity, leading to reactive oxygen species (ROS) overproduction. ROS further destabilize insulin signaling by oxidizing critical cysteine residues in IRS-1 and Akt, while simultaneously activating redox-sensitive kinases like JNK and IκB kinase β (IKKβ) [16, 17]. Lipid Toxicity: BPAF disrupts lipid homeostasis by upregulating DGAT2 (diacylglycerol acyltransferase 2) and downregulating PPARβ, promoting hepatic diacylglycerol (DAG) and ceramide accumulation. These lipid intermediates directly inhibit insulin receptor (IR) autophosphorylation and recruit protein kinase C epsilon (PKCε), which blocks insulin signaling [17,18].

Metabolic Crosstalk and Lipid-Mediated Stress

BPAF exacerbates systemic metabolic dysregulation through liver-adipose-pancreas crosstalk: Adipose Tissue Lipolysis: BPAF promotes adipocyte lipolysis, releasing free fatty acids (FFAs) and pro-inflammatory cytokines (e.g., TNF-α, IL-6) into circulation. FFAs activate Toll-like receptor 4 (TLR4) in hepatocytes, initiating NF-κB-driven inflammation and JNK/IKKβ signaling, which suppress IRS-1/2 [19,20]. Lipid-Laden Exosomes: Recent studies show that BPAF-enriched saturated fatty acids (SFAs) are packaged into small extracellular vesicles (sEVs). These sEVs deliver SFAs to hepatocytes, inducing lipotoxic stress, ER dysfunction, and TLR4-depen-

dent NF-κB activation, thereby amplifying insulin resistance [21]. Pancreatic β-Cell Dysfunction: BPAF downregulates pdx-1 and foxa2, impairing insulin secretion and exacerbating hyperglycemia. Elevated glucose further activates hepatic DAG-PKCε pathways, creating a vicious cycle of IR [17,21].

In this study, although there were no significant differences in liver weight and liver index (liver weight-to-body weight ratio) among the dose groups of C57BL/6J mice after 90 days of BPAF exposure ($P > 0.05$), Oil Red O staining revealed a significant increase in the number and size of lipid droplets in liver tissues with increasing BPAF doses. This indicates an increase in hepatic lipid accumulation. These results suggest that the increase in lipid accumulation may not be dependent on changes in liver weight. Localized Lipid Accumulation: Lipid accumulation may primarily occur in specific regions or cell types within the liver, rather than being evenly distributed throughout the liver tissue. This localized accumulation may not significantly affect the overall weight of the liver but can lead to metabolic changes at the cellular level. Dynamic Equilibrium of Lipid Accumulation: Despite increased lipid accumulation, the liver may maintain overall weight stability through other mechanisms, such as increased fatty acid oxidation or lipid transport. This dynamic equilibrium may mask the direct impact of lipid accumulation on liver weight. Adaptive Changes in the Liver: The liver may undergo adaptive changes, such as compensatory cell proliferation or changes in cell volume, to cope with lipid accumulation. These adaptive changes may help maintain the relative stability of liver weight. Such adaptations may include compensatory hepatocyte proliferation to maintain liver function.

Independence of Lipid Droplet Accumulation: The increase in lipid droplets may be independent of changes in liver weight. Lipid droplet formation and accumulation primarily reflect intracellular lipid metabolic disorders, while changes in liver weight may be more influenced by overall tissue structure and cell number. Therefore, the increase in lipid accumulation may more likely reflect intracellular metabolic changes rather than changes in the weight of the entire organ. Potential Pathophysiological Significance: The increase in lipid accumulation may be associated with potential liver dysfunction, even if liver weight does not significantly change. This lipid accumulation may lead to metabolic stress, oxidative stress, and inflammatory responses in hepatocytes, thereby affecting normal liver function. Future Research Directions: Future studies can further explore the relationship between lipid accumulation and liver weight, for example, through more detailed histological analysis, cellular-level metabolomics studies, and in-depth analysis of gene and protein expression related to lipid accumulation, to reveal the mechanisms and impact of lipid accumulation on liver function.

In summary, although there were no significant differences in liver weight, the increase in lipid accumulation suggests that BPAF exposure may have a significant impact on liver metabolism. This impact may be independent of changes in liver weight, reflecting intracellular lipid metabolic disorders and potential pathophysiological changes.

Inflammatory Amplification via Macrophage Polarization

BPAF skews hepatic and adipose tissue macrophages toward a pro-inflammatory M1 phenotype, driving chronic low-grade inflammation: M1 Macrophage Activation: BPAF upregulates macrophage chemoattractants (e.g., CCL2) and polarizes macrophages to an M1 state via TLR4/NF-κB signaling. M1 macrophages secrete TNF-α, IL-1β, and IL-6, which: Directly inhibit IR tyrosine kinase activity. Activate JNK/IKKβ to phosphorylate IRS-1/2 on serine residues. Suppress PPARγ, a transcriptional regulator of anti-inflammatory and insulin-sensitizing genes [19,20]. ER Stress-Inflammation Feedback Loop: ER stress in hepatocytes amplifies inflammation by releasing damage-associated molecular patterns (DAMPs), which activate NLRP3 inflammasomes in Kupffer cells (liver-resident macrophages). This results in caspase-1-mediated IL-1β maturation, further impairing insulin signaling [16]. Oxidative Stress and Lipid Peroxidation: BPAF-induced ROS enhance lipid peroxidation, generating pro-inflammatory mediators like 4-hydroxynonenal (4-HNE) and oxidized phospholipids. These molecules activate AP-1 and NF-κB, perpetuating inflammatory gene expression (e.g., TNF-α, IL-6) [18,22].

Integration of Pathways: A Feed-Forward Cycle

BPAF establishes a self-reinforcing cycle where MAMs dysfunction, lipid toxicity, and inflammation mutually exacerbate hepatic IR: ER Stress → JNK activation → IRS-1/2 inhibition → Impaired glucose uptake. Lipid Overload → DAG/PKCε and ceramide accumulation → IR desensitization. M1 Macrophage Polarization → TNF-α/IL-6 secretion → JNK/IKKβ activation → Further IRS-1/2 inhibition. ROS Overproduction → Oxidative damage → Inflammasome activation → IL-1β release. This interconnected network highlights BPAF's role as a metabolic disruptor that hijacks stress and inflammatory pathways to impair insulin action.

Therapeutic Implications

Targeting these pathways may mitigate BPAF-induced IR: MAMs Stabilizers: Compounds like resveratrol or chaperone inducers (e.g., TUDCA) to alleviate ER stress [23]. JNK/IKKβ Inhibitors: Pharmacological blockade of stress kinases (e.g., SP600125 for JNK). Macrophage Reprogramming: PPARγ agonists (e.g., rosiglitazone) to promote M2 polarization and suppress inflammation [18]. Antioxidants: N-acetylcysteine (NAC) to neutralize ROS and break the oxidative-inflammatory loop [17].

Conclusion

BPAF-induced hepatic insulin resistance arises from a triad of MAMs dysfunction, lipid-mediated metabolic cross-

talk, and macrophage-driven inflammation. These pathways converge on stress kinase activation (JNK/IKKβ), IRS-1/2 inhibition, and chronic inflammation, perpetuating a state of metabolic inflexibility. Future studies should explore tissue-specific epigenetic modifications (e.g., FoxO1 methylation) and inter-organ communication mechanisms to fully elucidate BPAF's diabetogenic potential.

Data Availability Statement

The datasets generated and analyzed during this study are available in the OMIX repository of the National Genomics Data Center (NGDC) under accession number [OMIX010050]. Additional supporting data are included in the article and its supplementary materials. For further inquiries, please contact the corresponding author.

Ethics Statement

The animal experiments were approved by the Shanghai Center for Disease Control and Prevention and the Shanghai Academy of Preventive Medicine. The study was conducted in accordance with local regulations and institutional requirements.

Author Contributions

Xin-yu Hong and Ning Wang were primarily responsible for conducting the experiments and collecting data regarding BPAF in the Transwell co-culture model and animal exposure experiments (investigation, data curation) and drafting the original manuscript (writing—original draft). They also participated in data analysis (formal analysis). Jing Leng, Da-sheng Lu, Jia-le Xu, Jing Xu, Xiao-qi Yu, Ke-lei Qian, Zhiqing Zheng and Gong-hua Tao made substantial contributions to the study on BPAF in metabolomics and animal exposure experiments, especially in the acquisition, analysis, and interpretation of experimental data.

Xin-yu Hong was responsible for reviewing and editing the final manuscript (writing—review & editing).

Corresponding author Ping Xiao contributed to the conception and design of the study (conceptualization) and contributed to the methodology. She was responsible for the administration of the project (project administration), provided necessary resources for the study (resources), and supervised the conduct of the research (supervision). In addition, she was responsible for obtaining funding for the study (funding acquisition).

All authors reviewed the final manuscript and agreed to submit this version. Corresponding author: Ping Xiao.

Funding

This study was supported by the Shanghai Natural Science Foundation, grant number 23ZR1459600; the Shanghai Public Health Three-Year Action Plan (2023-2025) Key Discipline Project, grant numbers GWVI-11.1-41 and 42; and the Shanghai Public Health Three-Year Action Plan (2023-2025) Project, grant number GWVI-4. The Institute of Chemical Safety Evaluation/State Environmental Protection Key Laboratory of Health Impact Assessment on New Environmental Pollutants at the Shanghai Center for Disease Control and Prevention provided the necessary facilities.

Conflict of Interest Statement

The authors declare that this study was conducted in the absence of any commercial or financial relationships that could be construed as potential conflicts of interest. Specifically, there was no commercial funding involved in this research.

Supplementary Materials

Metabolomics parameters:

In the HILIC analysis, an ACQUITY UPLC® BEH HILIC column (2.1×100 mm, 1.7 μm) was used, with the column temperature set at 35°C and an injection volume of 5 μL. The mobile phase consisted of solvent A (acetonitrile-water, 95/5, v/v, containing 10 mM ammonium acetate and 0.1% formic acid) and solvent B (acetonitrile-water, 50/50, v/v, containing 10 mM ammonium acetate and 0.1% formic acid). The elution conditions are detailed in Table 1. The gradient elution program was as follows: initially maintaining 99% solvent A for 2 minutes, then linearly decreasing to 45% solvent A over 6 minutes, subsequently increasing to 1% solvent A over 1 minute, and finally returning to the initial conditions within 0.1 minute. The flow rate was maintained at 0.4 mL/min for most of the run time, with a brief increase to 0.8 mL/min between 9.1 and 11.1 minutes.

Time(min)	Flow Rate(mL/min)	Solvent A(%)	Solvent B(%)
0	0.4	99	1
2	0.4	99	1
8	0.4	45	55
9	0.4	1	99
9.1	0.8	1	99
11	0.8	1	99
11.1	0.8	99	1
19	0.8	99	1
19.1	0.4	99	1
23	0.4	99	1

Table2: Elution Gradient for HILIC Analysis

The Orbitrap source parameters were optimized as follows: The sheath gas flow rate was set to 40 arb, the auxiliary gas

flow rate to 10 arb, and the sweep gas flow rate to 1 arb. The spray voltage was set to 3.3 kV in negative ion mode and 3.8 kV in positive ion mode. The capillary temperature was maintained at 320°C, and the S-lens RF level was set to 50.0 V. The auxiliary gas heater temperature was raised to 350°C. The mass spectrometer operated in full scan mode with a resolution of 70,000, an AGC target of 1e6, and a maximum ion time (IT) of 120 ms. The scan range was set between 55 and 825 m/z. For data-dependent MS2/MS3, the resolution was set to 17,500, the AGC target to 1e5, and the maximum IT to 50 ms. The isolation window was set to 1 m/z, and the normalized collision energy (NCE) was stepped at 30, 40, and 50. Dynamic exclusion was set to 6.0 s, the intensity threshold to 8.3e3, and the vertex trigger window ranged from 2 to 6 s. Charge exclusion settings were applied to exclude charge species of 2 to 8 and greater than 8. Isotopic exclusion was enabled.

Each batch of samples included at least one solvent blank and one process blank. The solvent blank, which was the re-dissolution solution used for sample analysis, was used to evaluate background contamination of the testing instrument and cross-contamination between samples. The process blank, which was prepared without adding sample matrix but otherwise underwent the same sample pretreatment and instrumental analysis as the samples, was used to evaluate contamination throughout the entire experimental process and for background subtraction during sample data filtering.

The QC sample was a pooled injection solution of the samples used in that batch (both experimental and control samples) and was used to evaluate the stability of the samples throughout the instrumental analysis and for sample data filtering. The diluted QC samples, which were 2-, 5-, and 10-fold dilutions of the QC sample with the re-dissolution solution used for sample analysis, were used to evaluate whether metabolites at different concentration levels exhibited severe matrix suppression or enhancement effects and to ensure that the sample concentration levels were within the dynamic response range of the instrument, which was also used for sample data filtering. Metabolite identification (MetID) was derived from pooled samples of the same category (same dosing level). All prepared samples were stored in a -20°C freezer.

Reference

1. Escrivá, Laura, Johanna Zilliacus, Ellen Hessel, and Anna Beronius. “Assessment of the endocrine disrupting properties of bisphenol AF: a case study applying the European regulatory criteria and guidance.” *Environmental Health* 20, no. 1 (2021): 48.
2. Karolinska Institutet, Institute of Environmental Medicine, Sweden, Laura Escrivá, Annika Hanberg, Johanna Zilliacus, and Anna Beronius. “Assessment of the endocrine disrupting properties of Bisphenol AF according to the EU criteria and ECHA/EFSA guidance.” *EFSA Journal* 17 (2019): e170914
3. Guan, Tianzhu, Yonghai Sun, Tiehua Zhang, Tiezhu Li, Zhuolin Li, Yue Zhang, Jie Zhang, and Yongjun Wang. “Simultaneous determination of bisphenol A and its halogenated analogues in soil by fluorescence polarization assay.” *Journal of soils and sediments* 18 (2018): 845-851..
4. Zhang, Yu, Zhi Xia, Guofeng Gui, Ping Zhang, Qianzhu Li, and Lifen Meng. “Graphdiyne-templated platinum nanoparticles as a novel platform for the electrochemical determination of bisphenol AF.” *Chemosensors* 10, no. 11 (2022): 485.
5. Matsushima, Ayami, Xiaohui Liu, Hiroyuki Okada, Miki Shimohigashi, and Yasuyuki Shimohigashi. “Bisphenol AF is a full agonist for the estrogen receptor ERα but a highly specific antagonist for ERβ.” *Environmental health perspectives* 118, no. 9 (2010): 1267-1272.
6. Huang, Mingquan, Guangrui Pan, Guofeng Xu, Shuang Liu, and Meng Yang. “Comparative Study of Bisphenol A and Its Selected Analogues on the Induction of Mitochondrial Mass Loss and Apoptosis in Human Granulosa Cells.” *Journal of Health and Environmental Research* 7, no. 1 (2021): 1-6.
7. Li, Rongzhen, Shuai Liu, Wenhui Qiu, Feng Yang, Yi Zheng, Ying Xiong, Guanrong Li, and Chunmiao Zheng. “Transcriptomic analysis of bisphenol AF on early growth and development of zebrafish (Danio rerio) larvae.” *Environmental Science and Ecotechnology* 4 (2020): 100054.
8. Akash, Muhammad Sajid Hamid, Sumbal Rasheed, Kanwal Rehman, Muhammad Imran, and Mohammed A. Assiri. “Toxicological evaluation of bisphenol analogues: preventive measures and therapeutic interventions.” *RSC advances* 13, no. 31 (2023): 21613-21628.
9. İyigündoğdu, İrem, Aylin Üstündağ, and Yalçın Duydu. “Toxicological evaluation of bisphenol A and its analogues.” *Turkish journal of pharmaceutical sciences* 17, no. 4 (2020): 457.
10. Li, Huichen, Jiahao Gao, Yue Liu, Yujia Ding, Yusong Guo, Zhongduo Wang, Zhongdian Dong, and Ning Zhang. “Toxic Effects of Bisphenol AF Exposure on the Reproduction and Liver of Female Marine Medaka (Oryzias melastigma).” *Animals* 14, no. 2 (2024): 222.
11. Fritsche, Kristin, Andrea Ziková-Kloas, Philip Marx-Stoelting, and Albert Braeuning. “Metabolism-disrupting chemicals affecting the liver: screening, testing, and molecular pathway identification.” *International Journal of Molecular Sciences* 24, no. 3 (2023): 2686.
12. Kolliniati, Ourania, Eleftheria Ieronymaki, Eleni Vergadi, and Christos Tsatsanis. “Metabolic regulation of macrophage activation.” *Journal of Innate Immunity* 14, no. 1 (2022): 51-68.

13. Blay-Cadanet, Julia, Alice Pedersen, and Christian Kanstrup Holm. "Cellular metabolites regulate central nucleic acid sensing pathways." *Frontiers in Immunology* 12 (2021): 635738.
14. Zeng, Wentao, Fei Li, Shikai Jin, Ping-Chih Ho, Pu-Ste Liu, and Xin Xie. "Functional polarization of tumor-associated macrophages dictated by metabolic reprogramming." *Journal of Experimental & Clinical Cancer Research* 42, no. 1 (2023): 245.
15. Karrer, Cecile, Thomas Roiss, Natalie von Goetz, Darja Gramec Skledar, Lucija Peterlin Mašič, and Konrad Hungerbühler. "Physiologically based pharmacokinetic (PBPK) modeling of the bisphenols BPA, BPS, BPF, and BPAF with new experimental metabolic parameters: comparing the pharmacokinetic behavior of BPA with its substitutes." *Environmental health perspectives* 126, no. 7 (2018): 077002.
16. Czaja, Mark J. "JNK regulation of hepatic manifestations of the metabolic syndrome." *Trends in Endocrinology & Metabolism* 21, no. 12 (2010): 707-713.
17. Czaja, Mark J. "Function of autophagy in nonalcoholic fatty liver disease." *Digestive diseases and sciences* 61 (2016): 1304-1313.
18. Odegaard, Justin I., and Ajay Chawla. "Alternative macrophage activation and metabolism." *Annual Review of Pathology: Mechanisms of Disease* 6, no. 1 (2011): 275-297.
19. Chawla, Ajay, Khoa D. Nguyen, and YP Sharon Goh. "Macrophage-mediated inflammation in metabolic disease." *Nature Reviews Immunology* 11, no. 11 (2011): 738-749.
20. Püschel, Gerhard Paul, Julia Klauder, and Janin Henkel. "Macrophages, low-grade inflammation, insulin resistance and hyperinsulinemia: a mutual ambiguous relationship in the development of metabolic diseases." *Journal of Clinical Medicine* 11, no. 15 (2022): 4358.
21. Garcia-Martinez, Irma, Rosa Alen, Laura Pereira, Adrián Povo-Retana, Alma M. Astudillo, Ana B. Hitos, Isabel Gomez-Hurtado et al. "Saturated fatty acid-enriched small extracellular vesicles mediate a crosstalk inducing liver inflammation and hepatocyte insulin resistance." *JHEP Reports* 5, no. 8 (2023): 100756.
22. Shoelson, S. E. "Lee j, Goldfine AB." Inflammation and insulin resistance. *J Clin Invest* 116, no. 7 (2006): 1793-1801.
23. Rieusset, Jennifer. "The role of endoplasmic reticulum-mitochondria contact sites in the control of glucose homeostasis: an update." *Cell death & disease* 9, no. 3 (2018): 388.

Citation: Ping Xiao, et.al. Mitochondrial-Associated Membranes-Succinate Mediated Hepatocyte-Macrophage Metabolic Crosstalk in BPAF-Induced Hepatic Insulin Resistance. J. Clin. Oncol. Rep. Vol 4, Iss 3. (2025). DOI: 10.58489/2836-5062/027